

# Topologically protected non-Hermitian super-volume-law entanglement

Wen-Tan Xue<sup>1</sup> and Ching Hua Lee<sup>1</sup>

<sup>1</sup>Department of Physics, National University of Singapore, Singapore 117542

The entanglement entropy encodes fundamental characteristics of quantum many-body systems, and is particularly subtle in non-Hermitian settings where eigenstates generically become non-orthogonal. In this work, we find that negative biorthogonal entanglement generically arises from topologically protected non-orthogonal edge states in free fermion systems, especially within topological flat bands. Departing from previous literature which associated negative entanglement with exceptional gapless points, we show that robustly negative entanglement can still occur in gapped systems. Gapless 2D topological flat bands, however, exhibits novel  $S_A \sim -\frac{1}{2}L_y^2 \log L$  super-volume-law entanglement behavior which scales quadratically with the transverse dimension  $L_y$ , independent of system parameters. This dramatically negative scaling can be traced to a new mechanism known as non-Hermitian critical skin compression (nHCSC), where topological and skin localization in one direction produces a hierarchy of extensively many probability non-conserving entanglement eigenstates across a cut in another direction. Our discovery sheds light on new avenues where topology interplays with criticality and non-Hermitian localization, unrelated to traditional notions of topological entanglement entropy. This topologically protected negative entanglement also manifests in the second Rényi entropy, which can be measured through SWAP operator expectation values.

The entanglement entropy plays a crucial role in unveiling fundamental insights into the locality of quantum information. For instance, by scaling either according to the volume or area [1–3], the entanglement entropy reveals whether quantum correlations pervade the entire system or remain localized. Intriguingly, numerous studies [4–6] have suggested that the presence of topological order can also be encoded in the entanglement entropy, as revealed by the presence of an additional constant term [7, 8] or discontinuities in the scaling relation.

In this work, we extend the study of entanglement entropy into the non-Hermitian regime [9–28], where a primary feature is that the eigenstates of the Hamiltonian  $H$  are generically non-orthogonal. To maintain orthogonality and preserve probabilistic interpretation of quantum mechanics, we employ a biorthogonal basis of left and right eigenstates—i.e.,  $H = \sum E_n |\psi_n^R\rangle\langle\psi_n^L|$  with  $\langle\psi_m^L|\psi_n^R\rangle = \delta_{mn}$  [29–33]. Within this biorthogonal framework, recent studies have revealed that both bipartite entanglement entropy and Rényi entropy can manifest unexpected negative values [34–38], attributable to the presence of geometric defectiveness at exceptional points (EPs) [35–38]. Building upon these insights, we uncover a new mechanism by which topology in non-Hermitian systems substantially influence entanglement entropy behavior. Specifically, we show that certain topological boundary states can exert a strongly non-local influence on the dominant entanglement behavior of the *entire* system, such as probability non-conservation leading to topologically protected negative free-fermion entanglement entropy.

Most notably, in our non-Hermitian model featuring topological flat bands, we uncover an unconventional negative super-volume-law entanglement scaling, given by  $S_A \sim -\frac{1}{2}L_y^2 \log L$ , where  $L$  and  $L_y$  are the system dimensions normal and parallel to the entanglement cut, respectively. This beyond-volume-law scaling reflects a novel quantum correlation structure that is fundamentally distinct from those observed in area-law and volume-law systems, and has rarely been reported in previous studies [39]. The enigmatic  $-L_y^2$  scaling dependence arises not just due to the enhanced non-

orthogonality of the states due to flatness of the band, but also the extensively many probability-nonconserving entanglement eigenstates that emerge due to the band criticality – in a new mechanism that we dub non-Hermitian critical skin compression (nHCSC).

Another key discovery of this work is that the presence of an EP is not strictly a prerequisite for observing negative entanglement entropy values – instead, substantial non-orthogonality among the right eigenstates suffices, and spectacularly so when the non-orthogonality is enforced by the topological flatband. We investigate two 2D topological non-Hermitian models where the topological edge states in these models demonstrate nearly perfect overlap, while the overlap among bulk states remains minimal. Remarkably, this enables topological nontriviality to be strategically employed to switch the negative entanglement entropy on or off.

## I. Results

### A. Negative entanglement from eigenstate non-orthogonality

In the non-Hermitian context, the density operator that preserves its role as a probabilistic weight is the biorthogonal density matrix  $\rho = |\Psi^R\rangle\langle\Psi^L|$ , where

$$|\Psi^R\rangle = \prod_{n \in \text{occ}} \psi_{Rn}^\dagger |0\rangle, \quad |\Psi^L\rangle = \prod_{n \in \text{occ}} \psi_{Ln}^\dagger |0\rangle \quad (1)$$

are the right and left many-body ground states created by bifermionic creation operators  $\psi_{Rn}^\dagger, \psi_{Ln}^\dagger$  satisfying  $\{\psi_{Ln}, \psi_{Rn}^\dagger\} = \delta_{mn}$ , such that  $\langle\Psi^L|\Psi^R\rangle = 1$ , even if  $\langle\Psi^R|\Psi^R\rangle \neq 1, \langle\Psi^L|\Psi^L\rangle \neq 1$ . We specialize to free boson and fermion systems, where the ground state and thermal states are Gaussian states. As such, all correlation functions adhere to Wick's theorem, and the reduced density matrix  $\rho_A$  corresponding to an entanglement subregion  $A$  is completely expressible [40] in terms of the two-point function  $\langle c_{x_1}^\dagger c_{x_2} \rangle = \langle x_1 | P | x_2 \rangle = L^{-1} \sum_k e^{ik(x_1-x_2)} P(k)$ , where [34]  $P(k) = \sum_{n \in \text{occ}} |\psi_n^R(k)\rangle\langle\psi_n^L(k)|$

projects to the occupied bands  $n$ , with  $k$  the momentum index. To enforce the entanglement cut, we also introduce  $\Gamma_A$  to be the real-space projector onto subregion  $A$ , such that the  $A$ -truncated band projector takes the form

$$\bar{P} = \Gamma_A P \Gamma_A = \sum_{n \in \text{occ}} \Gamma_A |\psi_n^R\rangle \langle \psi_n^L| \Gamma_A = \sum_{n \in \text{occ}} |\psi_{nA}^R\rangle \langle \psi_{nA}^L|. \quad (2)$$

Crucially, this  $\bar{P}$  operator contains complete information about the  $n$ th-order Rényi entropy for free fermions [41]

$$\begin{aligned} S_A^{(n)} &= \frac{\log \text{Tr}(\rho_A^n)}{1-n} = \frac{1}{1-n} \text{Tr} [\log (\bar{P}^n + (I - \bar{P})^n)] \\ &= \frac{1}{1-n} \sum_i \log (p_i^n + (1-p_i)^n), \end{aligned} \quad (3)$$

which, in the limit of  $n \rightarrow 1$ , yields the von Neumann entropy

$$\begin{aligned} S_A &= -\text{Tr} \rho_A \log \rho_A = -\text{Tr} [\bar{P} \log \bar{P} + (I - \bar{P}) \log (I - \bar{P})] \\ &= \sum_{p_i} -p_i \log(p_i) - (1-p_i) \log(1-p_i), \end{aligned} \quad (4)$$

where  $I$  is the identity matrix and  $p_i$  are the eigenvalues of  $\bar{P}$ . Physically, each  $p_i$  represents an occupation probability restricted to subregion  $A$ , and is real and bounded within  $[0, 1]$  for Hermitian Hamiltonian. In non-Hermitian settings, however,  $p_i$  can become complex and take values beyond  $[0, 1]$ , with magnitudes  $|p_i| \gg 1$ . This occurs due to the non-conservation of probability across the subregion boundary, as we shall demonstrate. Substituting such large  $|p_i|$  into Eqs (3) and (4) can result in an unexpected negative entanglement entropy. In general, both Rényi entropies  $S_A^{(n>1)}$  and von Neumann entropy  $S_A$  calculated from complex  $p_i$  can be complex. An important exception arises for PT-symmetric Hamiltonians, for which  $S_A^{(n)}$  remains real (see Methods, subsection C.2 for details). The topological flat band model [Eq (7)] discussed later, serves as a paradigmatic example. For more general cases, such as the exceptional crossing model in Eq (20), where  $\text{Im}(S_A^{(n)}) \neq 0$ , we show both the real and imaginary parts of the entropies, even though the the real part can be more directly measured.

Below, we show that mathematically, it suffices to have strong eigenstate overlap in order to have large  $|p_i|$ , which in turn results in negative Rényi and entanglement entropy. For any pair of non-orthogonal right eigenstates  $|\psi_m^R\rangle$  and  $|\psi_n^R\rangle$ , their normalized squared overlap [42]

$$\eta = \frac{|\langle \psi_m^R | \psi_n^R \rangle|^2}{\langle \psi_m^R | \psi_m^R \rangle \langle \psi_n^R | \psi_n^R \rangle} = \frac{(U^\dagger U)_{mn}^2}{(U^\dagger U)_{mm} (U^\dagger U)_{nn}} \neq 0 \quad (5)$$

does not vanish. Here we have introduced the matrix  $U$  whose elements are the real space components of the right eigenstates i.e.  $|\psi_n^R\rangle = \sum_i U_{in} |i\rangle$ , such that the corresponding matrix for the left eigenstates is  $U^{-1}$  i.e.  $\langle \psi_m^L | = \sum_i (U^{-1})_{mi} \langle i |$ . In the extreme limit where the two eigenstates become parallel,  $\eta \rightarrow 1$  and the rank of  $U$  becomes lower than the dimension of the space of occupied states. This leads to the vanishing of

$\text{Det}(U)$  and crucially forces  $U^{-1}$  to acquire very large matrix elements. From

$$\begin{aligned} \sum_{p_i} p_i^2 &= \text{Tr}(\bar{P}^2) = \sum_{m,n \in \text{occ}} \langle \psi_m^L | \Gamma_A | \psi_n^R \rangle \langle \psi_n^L | \Gamma_A | \psi_m^R \rangle \\ &= \sum_{m,n \in \text{occ}} (U^{-1} \Gamma_A U)_{mn} (U^{-1} \Gamma_A U)_{nm} \end{aligned} \quad (6)$$

where we have used  $\Gamma_A^2 = \Gamma_A$ , we deduce that at least one of the absolute values of  $p_i$  must also have become very large, since the divergent elements in  $U^{-1}$  do not in general cancel off with the small elements in  $\Gamma_A U$  except in the case of vanishing entanglement cut  $\Gamma_A = I$ . However, we stress that even when  $U$  is still full-rank with non-defective eigenspace,  $\eta$  can already be extremely close to unity and contribute to negative entanglement.

## B. Super-volume-law entanglement scaling induced by topological flat bands

In this section, we showcase a representative 2D system where topological edge states in flat bands (with  $\eta \approx 1$ ) give rise to negative entanglement entropy that scales with a super-volume-law. We consider a twisted [43] cylindrical geometry such that the  $y$  direction contains  $L_y$  unit cells, and is bounded so as to host topological edge states. The other translation-invariant (circumferential) direction contains  $L$  unit cells, and we shall assign half i.e.  $L/2$  of it to be the entanglement subregion  $A$ .  $P(k)$  projects onto the occupied lower half bands with  $\text{Re}[E(k)] < E_F = 0$  unless otherwise stated. To emphasize the cut direction, we label its unit cells and momentum as  $L$  and  $k$  instead of  $L_x$  and  $k_x$ . The key idea is that the non-Hermitian skin effect (NHSE) localizes all states towards a common boundary, such that the states would exhibit extremely high overlap if they are furthermore macroscopically energetically degenerate, as in the topological flat band. From our results below, this holds true even if the flat bands are not strictly gapless or defective.

To realize topologically protected flat bands across an extended range of  $k$ , it suffices to consider a minimal 2-component [44] Hamiltonian

$$H(k, k_y) = \begin{pmatrix} 0 & t e^{-ik_y} + a_0 \\ t e^{ik_y} + (b_0 - \cos k)^B & 0 \end{pmatrix}, \quad (7)$$

with  $k$ -dependent asymmetric off-diagonal hoppings, where  $a_0, b_0$  and hopping distance  $B > 0$  are all real. This structure guarantees that the entanglement entropy  $S_A$  remains real (see Methods, subsection C.2). Under OBCs in the  $y$ -direction, we treat the  $x$ -momentum  $k$  as a parameter, such that Eq (7) effectively describes a 1D non-Hermitian SSH model, previously well studied using the generalized Brillouin zone (GBZ) method [9, 15]. Therefore, we know that the NHSE results in boundary state localization with a skin depth of  $-2/\log[(b_0 - \cos k)^B/a_0]$  and dynamically induces a real energy spectrum from non-Bloch PT-symmetry [45–48]. Moreover, by computing the topological winding number defined

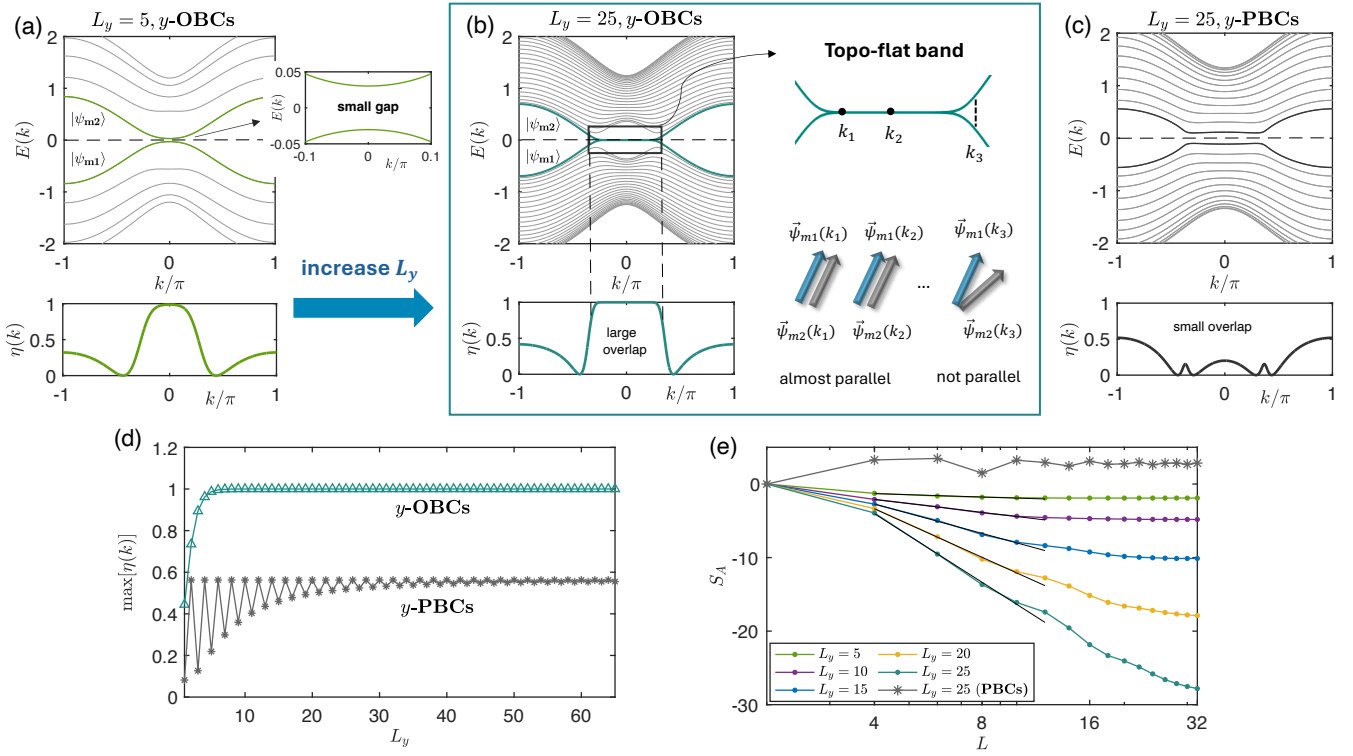


FIG. 1. Robustly negative entanglement entropy from the gapped topological flat bands of our 2-component Hamiltonian (Eq (7)), for parameters  $B = 1, t = 0.8, a_0 = 1$  (with  $b_0 = 1.2 \neq 1$  to open up the gap). (a) For small cylinder length  $L_y = 5$  and  $y$ -direction OBCs, the energy spectrum  $E(k)$  of the topological edge states  $|\psi_{m1}\rangle, |\psi_{m2}\rangle$  (bolded) exhibits a small but visible gap, but their overlap factor  $\eta(k)$  already approaches unity. (b) Upon increasing  $L_y$  to 25, a topological flat band with exponentially small gap is observed within the non-trivial regime prescribed by Eq (8), with  $\eta(k) \approx 1$  extremely closely. (c) With  $y$ -PBCs, the midgap flat band disappears and  $\eta(k)$  deviates markedly from unity, even though the gap is still small. (d) For  $y$ -OBCs but not  $y$ -PBCs, the overlap  $\eta(k)$  saturates very close to unity once  $L_y \sim 10^1$ . (e) The entanglement entropy scaling behavior  $S_A$  for different  $L_y$ . Notably, as  $L_y$  increases,  $S_A$  decreases with  $\log L$  more rapidly as  $S_A \sim -(\alpha L_y + \beta) \log L$ , with  $\alpha \approx 0.6633, \beta \approx -4.1817$  according to obtained from numerical fitting (black). It also saturates at  $S_{\min} \sim -L_y$  when  $L \gtrapprox L_y$ .

via integration over the GBZ, we find almost-flat topological bands existing whenever

$$|a_0(b_0 - \cos k)^B| \leq t^2, \quad (8)$$

as shown in Fig. 1(b). Due to finite-size effects, these topological bands are *not necessarily* gapless for any  $L_y$ , resulting in a dependence of band flatness—and hence the entanglement entropy—on  $L_y$ . Specifically, employing Schur's determinant identity on the real-space Hamiltonian  $[H_{y\text{-OBC}}(k)]_{y_1, y_2} = (2\pi)^{-1} \int e^{ik_y(y_1-y_2)} H(k, k_y) dk_y$ , as elaborated in Methods, subsection B.1, we obtain

$$\det[H_{y\text{-OBC}}(k)] = [a_0(b_0 - \cos k)^B]^{L_y}, \quad (9)$$

and consequently, the energies  $E_{e_1}(k)$  and  $E_{e_2}(k)$  of the two topological edge modes satisfy:

$$E_{e_1}(k)E_{e_2}(k) \approx \left[ \frac{a_0(b_0 - \cos k)^B}{t^2} \right]^{L_y}. \quad (10)$$

This implies that the topological gap also exhibits an inverse exponential scaling,  $\Delta = 2|E_{e_1}| \sim (\text{Const.})^{-BL_y}$ , which vanishes as  $L_y \rightarrow \infty$ , as derived in Methods subsection B.1, even

though it never exactly closes. Accordingly, the band flatness depends exponentially on  $BL_y$ . Perfect gap closure is only possible for  $|b_0| \leq 1$ , and below we investigate these two cases separately.

1. *Gapped topological flat bands ( $b_0 > 1$ )*.—Even though the topological bands are gapped, they become almost flat and touching as  $L_y$  is increased, as depicted in Figs. 1(a,b). At large  $L_y$ , their gap becomes exponentially small within the topologically non-trivial region given by Eq (10), where the overlap factor  $\eta(k) \approx 1$ , indicating that  $|\psi_{m1}\rangle$  and  $|\psi_{m2}\rangle$  are nearly parallel. This suggests that states within an extensive continuum of  $k$  closely approximate EPs, which is unexpected since the Hamiltonian  $H(k, k_y)$  in Eq (7) does not inherently feature EP crossings. As a comparison, for periodic boundary conditions(PBCs) in the  $y$  direction [Fig. 1(c)], the topological flat band is absent, and the overlap  $\eta(k)$  does not approach 1 even as  $L_y$  increased to a large value of 25 where the (bulk) band gap becomes quite narrow. For  $y$ -OBCs, even at very small  $L_y \approx 5$  number of layers,  $\eta(k)$  is already very close to one [Fig. 1(d)]; at larger  $L_y$ ,  $\eta(k)$  converges exponentially to 1 despite the system being physically gapped.

This strong topological flat band-induced non-orthogonality ( $\eta \approx 1$ ) is manifested in a strongly negative

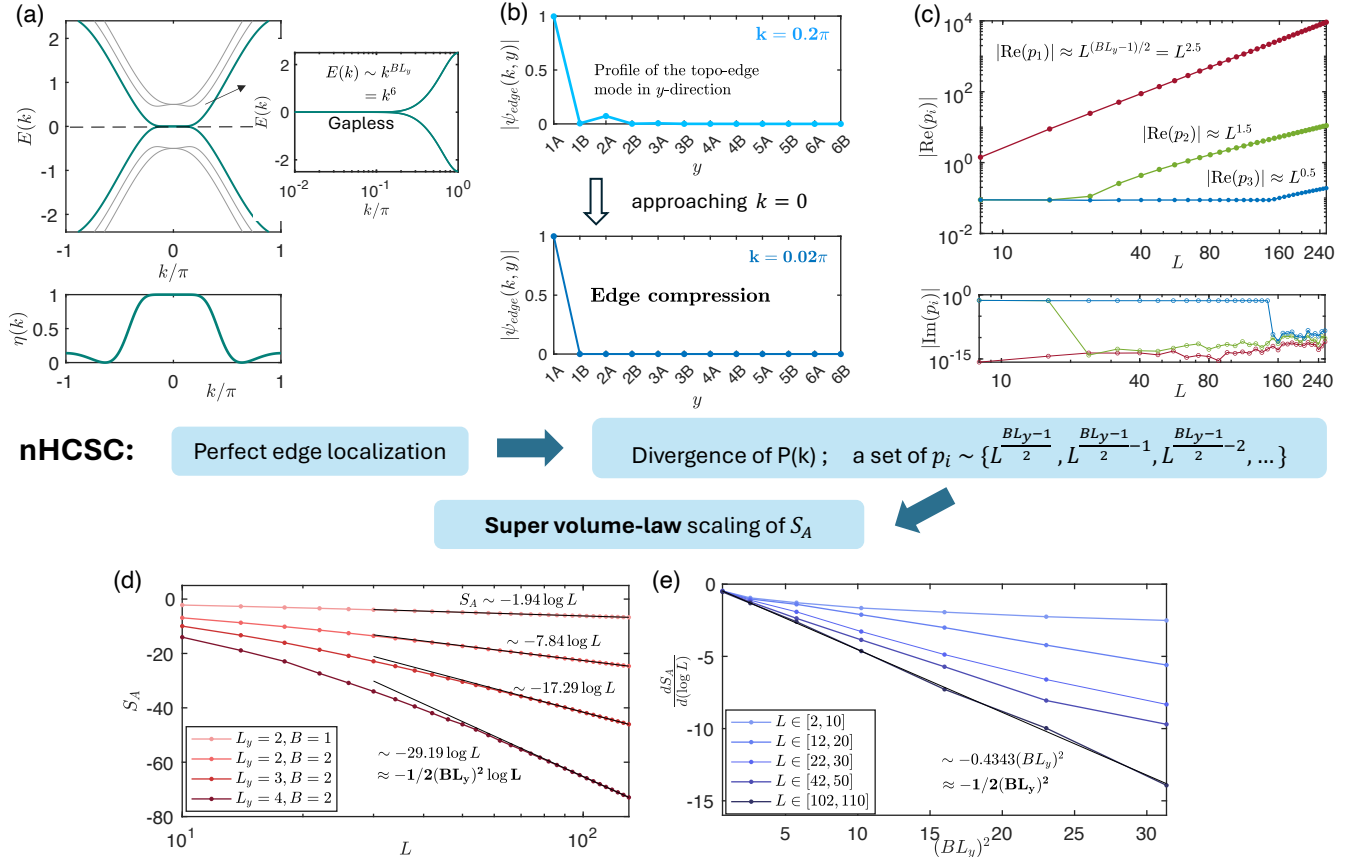


FIG. 2. Very robustly super-volume-law negative entanglement entropy  $S_A$  from gapless topological flat bands of our 2-component Hamiltonian (Eq (7)) with parameters  $b_0 = 1, t = 0.5, a_0 = 2$ . (a) Even for small  $L_y = 3, B = 2$ , a topological gapless flat band (boldest) with dispersion  $E_e(k) \sim k^{BL_y}$  and overlap  $\eta(k) \approx 1$  emerges around  $k = 0$  under  $y$ -OBCs. (b) As  $k$  approaches 0, the skin effect ( $r(k) \rightarrow 0$ ) strongly compresses the topological eigenstate onto site 1A, leading to nearly perfect localization. (c) For this gapless case, occupancy eigenvalues  $p_i$  (Eq (12)) of  $\tilde{P}$  dramatically exceed the  $[0, 1]$  interval due to non-Hermitian critical skin compression (nHCSC), with  $p_1, p_2, p_3, \dots$  (red, green, blue...) exhibiting a hierarchy of power-law dependencies with  $L$ . (d) The negative entanglement scaling is accurately approximated by  $S_A \approx -\frac{1}{2}(BL_y)^2 \log L$  (Eq (13), black) across different  $B, L_y$  combinations for sufficiently large cylinder circumference  $L$ . This is manifestly super-volume-law behavior with respect to the cylinder length  $L_y$ . (e) The coefficient of  $\log L$  in the numerical  $S_A$ , extracted through the gradient of the  $dS_A/d(\log L)$  plots (shades of blue), agrees well with  $-\frac{1}{2}(BL_y)^2$  (Eq (13)) when  $L \gtrsim 10^2$ . At smaller  $L$ , super-volume-law dependence  $\propto (BL_y)^2$  still holds for smaller  $BL_y$ , albeit with a smaller coefficient.

bipartite entanglement entropy  $S_A$ . As shown in Fig. 1(e),  $S_A$  scales negatively with the cylinder circumference  $\log L$ , with a gradient that grows with its length  $L_y$ . From Methods, subsection B.3, the exact dependence is established as  $S_A \sim -(\alpha L_y + \beta) \log L$ , where  $\alpha \approx 0.6633, \beta \approx -4.1817$  as obtained from numerical fitting. Notably, this linear dependence on  $L_y$  does *not* arise trivially because the length of the entanglement cut scales with  $L_y$ , since it is contributed only by the topological modes whose number do not scale extensively with system length. Rather, it arises because the band flatness scales exponentially with  $L_y$ . That said, for a given  $L_y$ , the entanglement entropy  $S_A$  saturates at negative lower bound (Methods, subsection B.3)  $S_{\min} \sim -L_y \log[a_0(b_0 - 1)^{-B}]$  because the system is ultimately gapped, such that the overlap  $\eta$  at  $k_0 = \pi/L$  (nearest point to  $k = 0$ ) does not approach arbitrarily close to 1 with increasing  $L$ . For PBCs, the bulk gap also results in the saturation of  $S_A$  at a positive value, as

depicted by the starred grey trend in Fig. 1(e).

**2. Gapless topological flat bands ( $b_0 = 1$ ) with super-volume-law negative entanglement.** – Finally, we discuss the most intriguing case where  $\det[H_{y\text{-OBC}}(k)] = 0$  at  $k = 0$  [Eq (9)], such that the topological band gap vanishes exactly [Fig. 2(a)]. Even though its band structure looks superficially similar to the  $b_0 > 1$  case with exponentially small gap [Fig. 1], its entanglement entropy exhibits a surprising super-volume-law dependence  $S_A \sim -\frac{1}{2}B^2 L_y^2 \log L$ , proportional not to the cylinder length  $L_y$ , but to the *square* of it. While the first power of  $L_y$  can be attributed to the exponentially high topological band flatness as before, the additional second power of  $L_y$  emerges from an uniquely new 2D phenomenon which we call non-Hermitian critical skin compression (nHCSC).

To understand the nHCSC, recall that all states are pushed to the cylinder's edges due to the  $y$ -hopping asymmetry in our model Eq (7). In particular, the left and right biorthogonal

topological eigenstates exhibit exponential spatial- $y$  profiles  $|\psi_{edge}^L(k, y)| \sim r(k)^{-y}$  and  $|\psi_{edge}^R(k, y)\rangle \sim r(k)^y$  with  $r(k) = \sqrt{(1 - \cos k)^B/a_0} < 1$ , and are localized at edges  $y = L_y$  and  $y = 1$ , respectively. Since these are the two eigenstates that exhibit the highest overlap  $\eta(k)$ , they dominate the entanglement contribution in  $\tilde{P}$ . Due to their criticality (gaplessness),  $r(0) = 0$  and the state is perfectly skin-localized (see Fig. 2(b)) for the  $k = 0$  topological mode in the  $x$ -direction along the cylinder edge.

Ordinarily, this perfect edge localization (or “compression”) only leads to irreversible 1D non-Bloch dynamics [49] and singular generalized Brillouin zones [50–52]. However, in our 2D topological entanglement context, it also causes the occupied band projector

$$[P(k)]_{y, y'} \approx |\psi_{edge}^R(k, y)\rangle \langle \psi_{edge}^L(k, y')| \sim r(k)^{y-y'} \quad (11)$$

to diverge for matrix blocks  $y < y'$ , with strongest divergence in  $[P(k)]_{1, L_y} \sim r(k)^{-L_y} \sim (1 - \cos k)^{-BL_y/2}$ . Notably, the most strongly divergent contribution  $\sim k^{-BL_y}$  from  $(1 - \cos k)^{-BL_y/2}$  does *not* dominate the total negative entanglement; of also substantial significance are the entire set of divergent terms  $k^{-BL_y+2}, k^{-BL_y+4}, k^{-BL_y+6}, \dots$  from the sub-leading terms in the expansion of  $(1 - \cos k)^{-BL_y/2}$ , as well as other  $[P(k)]_{y, y'}$  (see Methods, subsection B.2). Consequently, distinct from ordinary EP crossings [34, 35], essentially the *entire* set of  $\tilde{P}$  eigenvalues  $p_i$ , diverges with  $L$ :

$$p_i \approx \text{Re}(p_i) \sim \{L^{\frac{BL_y-1}{2}}, L^{\frac{BL_y-1}{2}-1}, L^{\frac{BL_y-1}{2}-2}, \dots\}, \quad (12)$$

where the imaginary parts  $\text{Im}(p_i)$  remain negligible, as shown in Fig. 2(c). This is the main consequence of nHCSC, which hinges on both the edge compression of the eigenstates and its criticality (vanishing of  $r(k)$ ). The hierarchy of these divergent occupancy eigenvalues is shown in Fig. 2(c): upon closer inspection, subdominant  $p_2, p_3 \sim L^{\frac{BL_y-1}{2}-1}, L^{\frac{BL_y-1}{2}-2}$  eigenvalues (green, blue) are observed in addition to the dominant  $p_1 \sim L^{\frac{BL_y-1}{2}}$ . Summing over them, the total entanglement entropy scales like (Methods, B.2)

$$\begin{aligned} S_A &= - \sum_{p_i} p_i \log p_i + (1 - p_i) \log(1 - p_i) \\ &\approx - \left[ \frac{BL_y - 1}{2} + \left( \frac{BL_y - 1}{2} - 1 \right) + \left( \frac{BL_y - 1}{2} - 2 \right) + \dots \right] \log L \\ &\approx -\frac{1}{2}(BL_y)^2 \log L. \end{aligned} \quad (13)$$

This strongly negative entanglement  $S_A$  is plotted in Fig. 2(d) for various  $B, L_y$ , and can be as low as  $-70$  for reasonably large  $L_y = 4, B = 2$ . By examining the slope of  $S_A$  with respect to the universal  $\log L$  factor, it is numerically confirmed in Fig. 2(e) that the super-volume-law quadratic coefficient  $-(BL_y)^2/2$  accurately holds for across a wide range of  $BL_y$  as long as  $L \gtrsim 10^2$  (even though moderately large  $L \sim \mathcal{O}(10)$  suffices when  $BL_y$  is also of  $\mathcal{O}(10)$ ).

### C. Prospects for measuring negative entanglement through the second Rényi entropy

As established in subsection C.1 of the Methods, the negative entanglement also manifests generically as negative Rényi entropy. Below, we outline a scheme for measuring the second Rényi entropy, defined in the biorthogonal basis as:

$$S_A^{(2)} = -\log \text{Tr}[(\rho_A)^2], \quad (14)$$

where the reduced density matrix is given by  $\rho_A = \text{Tr}_{\bar{A}}[|\Psi^R\rangle \langle \Psi^L|]$ .

A known approach [53–55] for measuring the second Rényi entropy or quantum purity involves the SWAP operator, which exchanges two copies of a quantum state:

$$\text{SWAP}|\psi_1\rangle \otimes |\psi_2\rangle = |\psi_2\rangle \otimes |\psi_1\rangle. \quad (15)$$

A commonly used corollary [56] is  $\text{Tr}(\text{SWAP}\rho_1 \otimes \rho_2) = \text{Tr}(\rho_1\rho_2)$ , from which the second Rényi entropy can be calculated from the expectation value of the SWAP operator on two-copies of the many body state [57] as:

$$\begin{aligned} \langle \psi | \otimes \langle \psi | \text{SWAP}_A |\psi\rangle \otimes |\psi\rangle &= \text{Tr}(\text{SWAP}_A \rho \otimes \rho) \\ &= \text{Tr}(\rho_A^2) = e^{-S_A^{(2)}}, \end{aligned} \quad (16)$$

where  $\text{SWAP}_A$  denotes the application of the SWAP operator in subregion  $A$ . Substituting  $\rho = |\Psi^R\rangle \langle \Psi^L|$ , we obtain

$$\begin{aligned} \langle \Psi^L | \otimes \langle \Psi^L | \text{SWAP}_A |\Psi^R\rangle \otimes |\Psi^R\rangle &= e^{-S_A^{(2)}} \\ |\langle \Psi^L | \otimes \langle \Psi^L | \text{SWAP}_A |\Psi^R\rangle \otimes |\Psi^R\rangle| &= e^{-\text{Re}[S_A^{(2)}]}. \end{aligned} \quad (17)$$

Therefore, to measure the (real part of the) biorthogonal second Rényi entropy,  $\text{Re}[S_A^{(2)}]$ , the most mathematically direct way would be to prepare two copies of the ground state of the Hamiltonian  $H$  as  $|\Psi^R\rangle \otimes |\Psi^R\rangle$ , applying the SWAP operator in subregion  $A$ , and then measuring its overlap with the ground state  $|\Psi^L\rangle \otimes |\Psi^L\rangle$  of another Hamiltonian  $H^\dagger$ . This approach could potentially be implemented using programmable quantum computers [58–61]. Post-selection, which has been used in measuring negative conditional entropy [62], will also be useful in simulating the non-Hermiticity [25, 63, 64].

Alternatively, it would usually be more practical to measure the physical (not biorthogonal) expectation values of the SWAP operator, either as:

$$\begin{aligned} \langle \text{SWAP}_A \rangle_{RR} &= \langle \Psi^R | \otimes \langle \Psi^R | \text{SWAP}_A |\Psi^R\rangle \otimes |\Psi^R\rangle, \\ &\text{or} \\ \langle \text{SWAP}_A \rangle_{LL} &= \langle \Psi^L | \otimes \langle \Psi^L | \text{SWAP}_A |\Psi^L\rangle \otimes |\Psi^L\rangle. \end{aligned} \quad (18)$$

Thus, to measure  $|\langle \Psi^L | \otimes \langle \Psi^L | \text{SWAP}_A |\Psi^R\rangle \otimes |\Psi^R\rangle|$  as given in Eq (17), one feasible strategy is to prepare a superposition state with known amplitudes  $c_1, c_2$  in a physical system:

$$|\Psi\rangle = c_1 |\Psi^R\rangle \otimes |\Psi^R\rangle + c_2 |\Psi^L\rangle \otimes |\Psi^L\rangle, \quad (19)$$

and then measure the expectation value  $\langle \Psi | \text{SWAP}_A |\Psi\rangle$ . The left-right overlap terms (i.e. Eq (17)) can subsequently be

calculated by subtracting the contributions from  $\langle \text{SWAP}_A \rangle_{RR}$  and  $\langle \text{SWAP}_A \rangle_{LL}$ , which can also be independently measured. Moreover, the OBC spectrum of our model, as specified in Eq. (9), is purely real, leading to identical energies for  $|\Psi^R\rangle$  and  $|\Psi^L\rangle$  and thus facilitating the preparation of their superposition.

Beyond the approach described above, other potentially feasible ways for observing negative entanglement can involve directly measuring the reduced density matrix to calculate the entanglement entropy through quantum state tomography [65–67], as well as measuring the non-local correlations in phononic crystals [68], from which the entanglement entropy can be inferred. Related quantum simulations through quantum Monte Carlo approaches [55, 69] and ultracold atomic optical lattices [53, 54, 70–72] can also reveal the associated quantum correlations.

#### D. Discussion

We have discovered a super-volume-law scaling of free fermion entanglement entropy in non-Hermitian, topologically non-trivial systems—particularly those featuring topological flat bands. Specifically, the entropy scales quadratically as  $S_A \sim -\frac{1}{2}L_y^2 \log L$ , despite the entanglement cut being only of length  $L_y$ . This highly unconventional scaling goes beyond the well known area and volume law, and to our knowledge, has no analogue in Hermitian systems. We identify the origin of this behavior as a new mechanism we call non-Hermitian critical skin compression (nHCSC), where the criticality of highly degenerate NHSE-compressed topological modes gives rise to an extensive hierarchy of probability non-conserving  $\tilde{P}$  eigenstates that gives rise to even stronger negative  $S_A$ . Moreover, we find that this negative scaling feature relies on substantial eigenstate overlap around the Fermi surface, which is less stringent than the previously suggested requirement of an exceptional crossing [34]. As such, macroscopically degenerate flatbands resulting from simultaneous topological and non-Hermitian skin localization can lead to strongly negative entanglement entropy, even in the presence of a small gap. Importantly, this negative entanglement also applies to the Rényi entropy which can be physically measured as suggested in previous subsection C, placing topology as a potentially practical control knob for probability non-conserving negative entanglement.

## II. Methods

### A. A comparative 4-band model with exceptional topological crossing

#### 1. Negative entanglement from exceptional topological crossing

In this section, we showcase a 4-band model featuring two topological edge modes that intersect at an exceptional crossing, rather than forming flat bands. We compare its entanglement scaling behavior with that of the flat-band model dis-

cussed in the Results, thereby providing a more comprehensive perspective on topologically protected negative entanglement. Unlike typical topological band crossings [73, 74] where the topological modes just have to be energetically degenerate, here we require them to also coalesce i.e. become parallel. A candidate model is given by the following 4-band Hamiltonian (see Methods, subsection A.2)

$$\begin{aligned} \mathcal{H}(k, k_y) = & (\cos k_y - \sin k - M)\tau_x\sigma_0 \\ & + \tau_y(\cos k\sigma_x - \sigma_y + \sin k_y\sigma_z) \\ & + (\sin \alpha\tau_0 + \cos \alpha\tau_x) \sum_{\mu=x,y,z} \sigma_\mu + i\delta\tau_y\sigma_0. \end{aligned} \quad (20)$$

where the  $\sigma_\mu$  and  $\tau_\mu$  Pauli matrices act in spin and sublattice space respectively. The first term controls the band inversion through  $M$ , the second term represents the spin-orbit coupling which break time-reversal, and the third term introduces a Zeeman field that can also involve sublattice hoppings. The final term,  $i\delta\tau_y\sigma_0$ , introduces non-Hermiticity through sublattice hopping asymmetry.

In Fig. 3, we present three distinct scenarios corresponding to different parameter combinations, focusing particularly on the overlap  $\eta(k)$  between the middle two eigenstates which straddle the Fermi energy  $E_F = 0$  (dashed line). Open boundary conditions (OBCs) are taken only along the  $y$  direction, such that  $k$  remains a good quantum number. In Fig. 3(a) with intersecting Hermitian topological modes (blue),  $\eta(k) = 0$  due to the exact orthonormality of Hermitian eigenstates. In Fig. 3(b) which is non-Hermitian ( $\delta \neq 0$ ),  $\eta(k)$  remains essentially zero due to the substantial line gap along  $\text{Re}(E) = 0$ . However, in the non-Hermitian case with topological modes [Fig. 3(c)], the topological edge modes (red) cross and coalesce, forming an exceptional point, as reflected by the saturated squared overlap of  $\eta(0) = 1$ . Only for this exceptional topological case do we see negatively entanglement entropy  $\text{Re}(S_A)$  [Fig. 3(d)]; for the previous two gapless and gapped cases of Figs. 3(a,b),  $\text{Re}(S_A)$  respectively grows/saturates with  $L$  as expected from usual conformal field theory [75–77].

Empirically, the

$$\text{Re}(S_A) \sim -0.3399 \log L \approx \left(\frac{1}{3} - \frac{2}{3}\right) \log L, \quad (21)$$

scaling in the exceptional topological case differs from the previously reported  $S_A \sim -\frac{2}{3} \log L$  scaling for a linearly dispersive exceptional point [34–36]. This discrepancy is attributed to non-exceptional gapless crossing [gray in Fig. 3(c)], which contributes the usual  $\frac{1}{3} \log L$  entanglement. As such, the negative entanglement from exceptional topological crossings can be easily overshadowed by other non-exceptional topological crossings, and is in this sense not necessarily robust [78].

#### 2. General form of the Hamiltonian and the EP in its bulk bands

Here, we show how the 4-band exceptional topological model given by Eq. (7) of the main text belongs to a more general

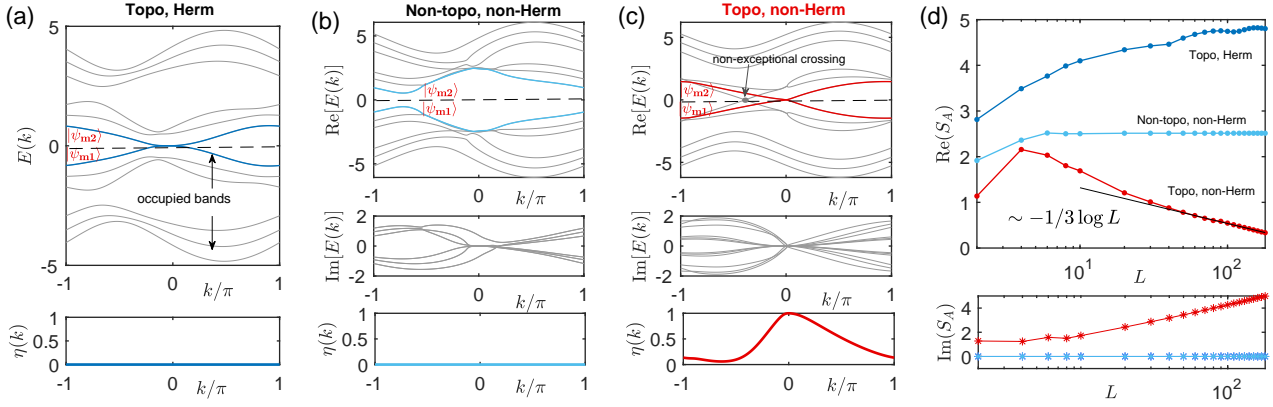


FIG. 3. Negative entanglement in the 4-band exceptional topological crossing model (Eq (20)) under y-OBCs with  $L_y = 3$ . (a) In the topologically non-trivial but Hermitian case ( $\alpha = 0, M = 1.2, \delta = 0$ ), the squared overlap  $\eta(k)$  [Eq (5)] of the topological eigenstates (blue) vanishes rigorously. (b) In the topologically trivial (line-gapped along  $\text{Re}(E) = 0$ ), non-Hermitian case ( $\alpha = 0.5\pi, M = 3, \delta = 2$ ),  $\eta(k)$  of the closest bulk states (light blue) still vanishes essentially. (c) For the non-trivial Chern case ( $\alpha = 0, M = 3, \delta = 2$ ), perfect overlap i.e.  $\eta(k) = 1$  is reached where topological edge modes (red) cross. (d) The free fermion entanglement entropy  $S_A$  (considering only the real part) for cases (a,b) respectively increases and saturates with system circumference  $L$  as expected, but that from the topological exceptional crossing (c) exhibits a new  $-\frac{1}{3} \log L$  scaling. The entanglement subregion is taken to be the half-cylinder with width  $L/2$ .

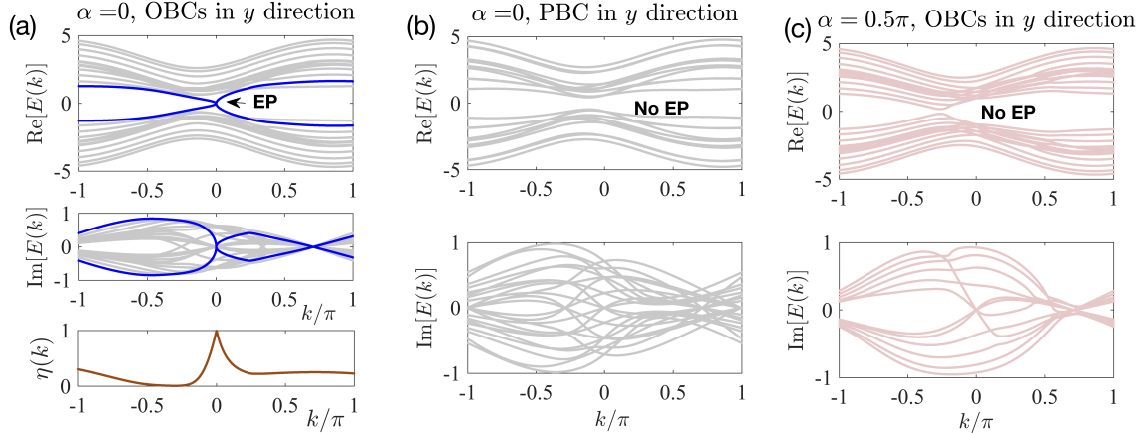


FIG. 4. Parameter and boundary dependence of EPs in our 4-band model given by Eq. (24). (a) For  $\alpha = 0$  and OBCs in the y direction, an EP occurs at  $k = 0$ . (b) With PBC in the y direction, no EP is observed, implying that the EP arises due to boundary localization. (c) For  $\alpha = \pi/2$  with OBCs in the y direction, no EP exists either. Other parameters:  $L_y = 6, M = 3, Z = 0.44, \lambda = \delta = 1$ .

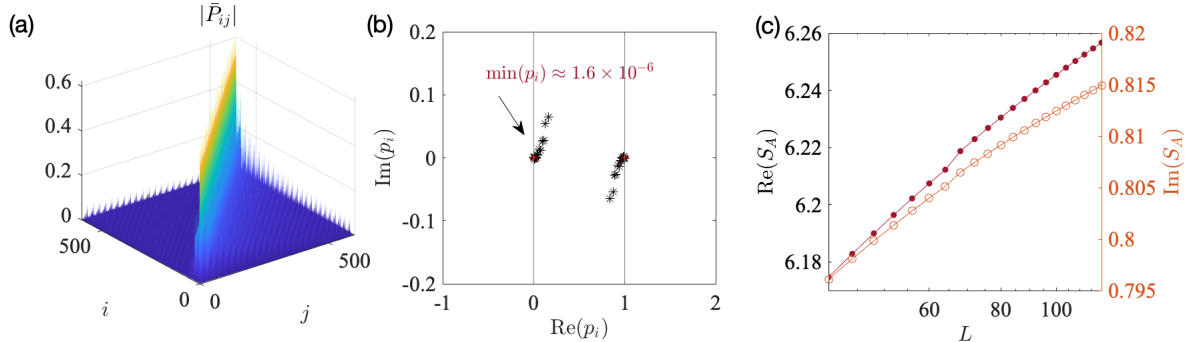


FIG. 5. Absence of (a) divergent truncated projector  $\bar{P}$  matrix elements and (b) eigenvalues outside of  $[0, 1]$  for an EP with square-root singularities. (c) Consequently, the real part of the entanglement entropy  $S_A$  does not exhibit any negativity. Parameters and model are the same as in Fig. 4(a), with  $x$ -direction size  $L = 50$  and  $L_y = 6$ .

family of extended exceptional topological models that exists three dimensions. A possible extension is [79]:

$$H(\mathbf{k}) = \left( \sum_{j=x,y,z} \cos k_j - M \right) \tau_z \sigma_0 + \lambda \sum_{j=x,y,z} \sin k_j \tau_x \sigma_j + [\sin \alpha \tau_0 + \cos \alpha \tau_z] (\vec{Z} \cdot \vec{\sigma}) + i \delta \tau_x \sigma_0 \quad (22)$$

where  $\lambda$  represents the strength of spin-orbit coupling, and  $\vec{Z} = (Z, Z, Z)^T$  is the Zeeman field of magnitude  $\sqrt{3}Z$  in the  $(1, 1, 1)$  direction. Upon the substitution  $k_y = -k_0$  with  $k_0 = \arcsin(Z)$ , and relabeling  $k_x$  as  $k$ , the above reduces to

$$\begin{aligned} \mathcal{H}(k, k_z) = & (\cos k + \cos k_0 + \cos k_z - M) \tau_z \sigma_0 + \lambda (\sin k \tau_x \sigma_x \\ & + \sin(-k_0) \tau_x \sigma_y + \sin k_z \tau_x \sigma_z) + (\sin \alpha \tau_0 + \cos \alpha \tau_z) \vec{Z} \cdot \vec{\sigma} \\ & + i \delta \tau_x \sigma_0, \end{aligned} \quad (23)$$

To simplify the notation, we further relabel  $k_z$  as  $k_y$ , apply a rotation to the Pauli matrices as  $\tau_x \rightarrow \tau_y \rightarrow \tau_z \rightarrow \tau_x$  and shift the spectrum by substituting  $k \rightarrow k + k_0$ , yielding the Hamiltonian:

$$\begin{aligned} H(k, k_y) = & (\cos(k + k_0) + \cos k_0 + \cos k_y - M) \tau_x \sigma_0 \\ & + \lambda (\sin(k + k_0) \tau_y \sigma_x + \sin(-k_0) \tau_y \sigma_y + \sin k_y \tau_y \sigma_z) \\ & + (\sin \alpha \tau_0 + \cos \alpha \tau_x) \vec{Z} \cdot \vec{\sigma} + i \delta \tau_y \sigma_0. \end{aligned} \quad (24)$$

Our model in Eq. (7) of the main text can be viewed as a specific instance of this generalized model that possesses the minimal ingredients of exceptional gapless topological modes, characterized by the parameters  $\lambda = 1, Z = 1$ , and  $k_0 = \arcsin(Z) = \pi/2$ .

### 2.1 Effect of EP dispersion on entanglement scaling

In Figs. 4 and 5, we aim to demonstrate that the presence of an exceptional points (EP), whether topologically protected or not, does not necessarily imply the occurrence of a negative EE; the outcome also depends on the energy dispersion around the EP. In Fig. 4(a,b), we present a topologically non-trivial configuration, characterized by blue lines that represent the topological edge states for only OBCs and not PBCs. As contrasted with the linear dispersion around the EP discussed in the main text, this scenario exhibits a square-root dispersion,  $E_e(k) \sim \sqrt{\delta k}$ .

Correspondingly, the overlap factor  $\eta(k) = |\langle \psi_m^R | \psi_n^R \rangle|^2 / [\langle \psi_m^R(k) | \psi_m^R(k) \rangle \langle \psi_n^R(k) | \psi_n^R(k) \rangle]$  between the two topological states indexed by  $m, n$  diminishes rapidly away from the EP  $k = 0$ . It should be noted that in a tight-binding model, the momentum  $k$  is discretized, with  $k_1 = \pi/L$  serving as the closest approximation to  $k = 0$ . Given the rapid decay of  $\eta(k)$  around  $k = 0$ , it follows that  $\eta(k_1)$  does not approach 1. Consequently, as observed in Fig. 5(a),  $\bar{P}$  exhibits only short-range hoppings, with its eigenvalues  $p_i$  almost all located within the range  $[0, 1]$  (Fig. 5(b)) just like for an ordinary non-exceptional model (other than the fact that  $p_i$  possess imaginary parts). Furthermore, the entanglement entropy remains positive and increases steadily with system size  $L$ , as shown in Fig. 5(c). Evidently, this

scenario with  $E_e(k) \sim \sqrt{\delta k}$  dispersion does not exhibit negative entanglement, suggesting that the dispersion around the EP crucially affects whether the entanglement entropy becomes negative. We will elaborate on how this dispersion can be tuned in our model in Methods, subsection A.3.

### 2.2 Effect of bulk states on entanglement scaling due to topological EPs

Returning to our model in Eq. (7) of the main text, we noted that EPs also exist in the bulk bands around  $\text{Re}[E(k)] \approx \pm 1.1$ . To investigate whether these bulk EPs could similarly induce a negative-valued entanglement entropy, we adjusted the Fermi energy to align with a bulk EP, setting  $E_F$  to 1.1. Observations from Fig. 6(a) indicate that the matrix elements of  $\bar{P}$  remain minimal, with  $p_i$  going beyond  $[0, 1]$  interval only around  $L = 90$  (see Fig. 6(b)). Consequently, the entanglement entropy exhibits a dip at this system size, albeit only a small dip. This occurs because the bulk EP is located at  $k' \approx 0.0106\pi$ , rather than at the long-wavelength limit  $k = 0$ . As  $L$  increases,  $k_1 = \pi/L$  will pass through the EP  $k'$ , inducing a dip in  $S_A$ . However,  $S_A$  generally remains positive and continues to increase with increasing  $L$ , indicating that the negative scaling observed in Fig. 1(d) of the main text must be predominantly a consequence of the EP in the topological edge bands crossing at  $k = 0$ , rather than of those within the bulk bands.

### 3. Deriving two types of dispersion relations (linear and square-root) for topological edge bands

For the general form of the Hamiltonian  $H(k, k_y)$  as defined in Eq (24), when considering OBCs in the  $y$ -direction with size  $L_y$ , we obtain:

$$H_{y\text{-OBC}}(k) = \begin{pmatrix} h_0^y & h_+^y & \cdots & 0 & 0 \\ h_-^y & h_0^y & h_+^y & \cdots & 0 \\ 0 & h_-^y & h_0^y & \cdots & 0 \\ \vdots & \vdots & \ddots & \ddots & \vdots \\ 0 & 0 & \cdots & h_-^y & h_0^y \end{pmatrix}_{L_y \times L_y}, \quad (25)$$

with

$$h_+^y = \begin{pmatrix} 0 & 0 & 0 & 0 \\ 0 & 0 & 0 & 1 \\ 1 & 0 & 0 & 0 \\ 0 & 0 & 0 & 0 \end{pmatrix}, h_-^y = \begin{pmatrix} 0 & 0 & 1 & 0 \\ 0 & 0 & 0 & 0 \\ 0 & 0 & 0 & 0 \\ 0 & 1 & 0 & 0 \end{pmatrix}, \text{ and } h_0^y(k) = \begin{pmatrix} 0 & R \\ L & 0 \end{pmatrix}, \quad (26)$$

where

$$\begin{aligned} R &= \begin{pmatrix} f + \delta + Z & 2Z - i(Z + \sin(k + k_0)) \\ i(Z - \sin(k + k_0)) & f + \delta - Z \end{pmatrix}, \\ L &= \begin{pmatrix} f - \delta + Z & -i(Z - \sin(k + k_0)) \\ 2Z + i(Z + \sin(k + k_0)) & f - \delta - Z \end{pmatrix}, \end{aligned} \quad (27)$$

and  $f = \cos(k + k_0) + \cos k_0 - M$ . For this  $H_{y\text{-OBC}}(k)$ , the topological edge bands exhibit two different types of dispersion relations around the EP: (1) a linear dispersion  $E_e(\delta k) \sim \delta k$ , as shown in Fig. 3(c), and (2) square-root dispersion  $E_e(\delta k) \sim \sqrt{\delta k}$ , as depicted in Fig. 4(a).

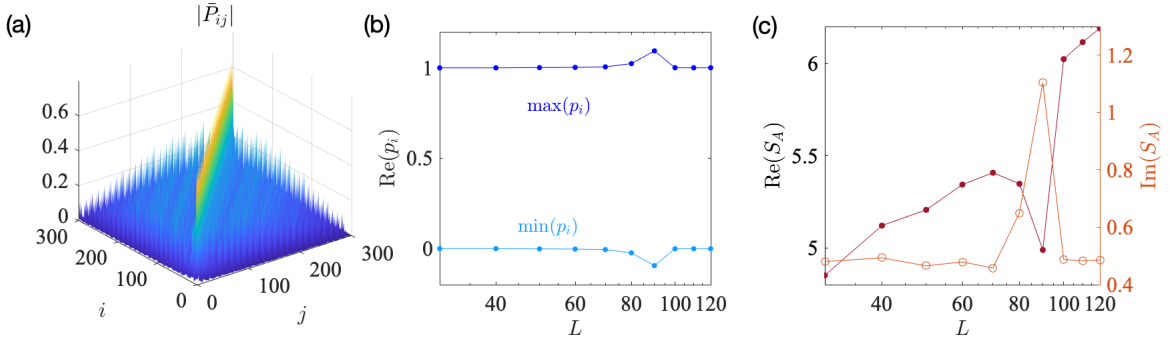


FIG. 6. Slight negative dip in the entanglement entropy due to bulk EPs. Shown is the model in Eq. (7) of the main text, with the Fermi Surface fixed at  $E_F = -1.1$  and parameters  $L_y = 3$ ,  $M = 3$  and  $\delta = 2$ . (a) The truncated projector  $\bar{P}$  matrix elements for  $L = 50$  with truncation at  $l = L/2 = 25$ . (b) The scaling of the maximum and minimum  $p_i$  with system size  $L$ , which goes out of the  $[0, 1]$  interval only around  $L = 90$ . (c) The real part of entanglement entropy  $S_A$  hence exhibits a slight negative dip at  $L \approx 90$ . However, this negative dip from the bulk EP is too weak to cause the entanglement to scale negatively as a whole.

To explain why the dispersion can exhibit two qualitatively different behavior (i.e., becomes linear when we set  $Z = 1, \delta = M - Z$  in Eq (24)), we expand the momentum  $k$  around the EP as:  $k \rightarrow 0 + \delta k$ . We shall prove that:

$$\det[H_{y\text{-OBC}}(\delta k)] \sim \begin{cases} \delta k^2, & \text{with } Z = 1, \delta = M - Z \\ \delta k, & \text{other parameters} \end{cases}. \quad (28)$$

This scaling behavior is directly linked to the dispersion of the topological bands, which are the only bands that become gapless in the spectrum. To elaborate, we know that the determinant is equal to the product of all eigenenergies as:

$$\det[H_{y\text{-OBC}}(k)] = E_{e_1}(k)E_{e_2}(k) \prod_n E_n(k), \quad (29)$$

where  $E_{e_1}(k)$  and  $E_{e_2}(k)$  are the two topological edge bands, and the  $E_n(k)$ s represent bulk bands. As  $\delta k \rightarrow 0$ ,  $\det[H_{y\text{-OBC}}(\delta k)]$  approaches zero, as do  $E_{e_1}(\delta k)$  and  $E_{e_2}(\delta k)$  with  $|E_{e_1}| = |E_{e_2}|$ . However, the bulk bands  $E_n(\delta k)$  approach finite values. Thus, the topological edge bands exhibit dispersions described by  $E_{e_{1,2}} \sim \sqrt{\det(H_{y\text{-OBC}})}$ . Below, we show that this  $\sim \delta k$  when the parameters are set to  $Z = 1, \delta = M - Z$ . For other parameter combinations,  $E_{e_{1,2}}$  will behave generically as  $\sim \sqrt{\delta k}$ .

To derive Eq (28), we first expand  $H_{y\text{-OBC}}$  around  $k = 0$ . Since  $k$  appears only in the diagonal element  $h_0^y$ , we need to expand the  $R$  and  $L$  matrices [Eq (27)]. By substituting  $\sin k_0 = Z$  into Eq (27), we obtain

$$\begin{aligned} \sin(k_0 + \delta k) &\approx Z + \cos k_0 \delta k - \frac{Z}{2} \delta k^2, \\ \cos(k_0 + \delta k) &\approx \cos k_0 - Z \delta k - \frac{\cos k_0}{2} \delta k^2, \end{aligned} \quad (30)$$

and

$$\begin{aligned} R(\delta k) &= \begin{pmatrix} R_{11} & R_{12} \\ R_{21} & R_{22} \end{pmatrix} \\ &= \begin{pmatrix} f_0 + \delta + Z & 2Z(1 - i) \\ 0 & f_0 + \delta - Z \end{pmatrix} + \begin{pmatrix} -Z & -i \cos k_0 \\ -i \cos k_0 & -Z \end{pmatrix} \delta k \\ &\quad + \begin{pmatrix} -\frac{1}{2} \cos k_0 & i \frac{Z}{2} \\ i \frac{Z}{2} & -\frac{1}{2} \cos k_0 \end{pmatrix} \delta k^2 + O(\delta k^3), \end{aligned} \quad (31)$$

where  $f_0 = 2 \cos k_0 - M$ , and

$$\begin{aligned} L(\delta k) &= \begin{pmatrix} L_{11} & L_{12} \\ L_{21} & L_{22} \end{pmatrix} \\ &= \begin{pmatrix} f_0 - \delta + Z & 0 \\ 2Z(1 + i) & f_0 - \delta - Z \end{pmatrix} + \begin{pmatrix} -Z & i \cos k_0 \\ i \cos k_0 & -Z \end{pmatrix} \delta k \\ &\quad + \begin{pmatrix} -\frac{1}{2} \cos k_0 & -i \frac{Z}{2} \\ -i \frac{Z}{2} & -\frac{1}{2} \cos k_0 \end{pmatrix} \delta k^2 + O(\delta k^3). \end{aligned} \quad (32)$$

Then, by using Schur's determinant identity,  $\det \begin{pmatrix} A & B \\ C & D \end{pmatrix} = \det(D) \det(A - BD^{-1}C)$  [80], we can calculate  $\det[H_{y\text{-OBC}}]$  as follows (for simplicity, we rewrite  $h_0^y$  as  $h_0$ ):

$$\begin{aligned} \det \begin{pmatrix} h_0 & h_+ & \cdots & 0 \\ h_- & h_0 & h_+ & \vdots \\ 0 & h_- & \ddots & h_+ \\ 0 & \cdots & h_- & h_0 \end{pmatrix}_{L_y} &= \det(h_0) \det \begin{pmatrix} h_0 & h_+ & \cdots & 0 \\ h_- & h_0 & h_+ & \vdots \\ 0 & h_- & \ddots & h_+ \\ 0 & \cdots & h_- & h_0^{(1)} \end{pmatrix}_{L_y-1} \\ &= \det(h_0) \det(h_0^{(1)}) \det \begin{pmatrix} h_0 & h_+ & \cdots & 0 \\ h_- & h_0 & h_+ & \vdots \\ 0 & h_- & \ddots & h_+ \\ 0 & \cdots & h_- & h_0^{(2)} \end{pmatrix}_{L_y-2} \\ &= \det(h_0) \det(h_0^{(1)}) \det(h_0^{(2)}) \cdots \det(h_0^{(L_y-1)}), \end{aligned} \quad (33)$$

in which  $h_0^{(1)} = h_0 - h_+ h_0^{-1} h_- = \begin{pmatrix} 0 & R^{(1)} \\ L^{(1)} & 0 \end{pmatrix}$ , with

$$R^{(1)} = R - \begin{pmatrix} 0 & 0 \\ (R^{-1})_{21} & 0 \end{pmatrix}, \quad L^{(1)} = L - \begin{pmatrix} 0 & (L^{-1})_{12} \\ 0 & 0 \end{pmatrix} \quad (34)$$

and  $h_0^{(2)} = h_0 - h_+ [h_0^{(1)}]^{-1} h_- = \begin{pmatrix} 0 & R^{(2)} \\ L^{(2)} & 0 \end{pmatrix}$ , with

$$R^{(2)} = R - \begin{pmatrix} 0 & 0 \\ [(R^{(1)})^{-1}]_{21} & 0 \end{pmatrix}, \quad L^{(2)} = L - \begin{pmatrix} 0 & [(L^{(1)})^{-1}]_{12} \\ 0 & 0 \end{pmatrix}, \quad (35)$$

and so forth  $h_0^{(n)} = h_0 - h_+ [h_0^{(n-1)}]^{-1} h_-$ . Now, to calculate Eq (33), we need to determine how  $\det(h_0^{(n)})$  varies with  $\delta k$ .

- For the case considered in the main text with  $\lambda = Z = 1, \delta = M - Z, k_0 = \pi/2$ , we have

$$\begin{aligned} R(\delta k) &= \begin{pmatrix} -\delta k & 2(1-i) + \frac{i}{2}\delta k^2 \\ \frac{i}{2}\delta k^2 & -2 - \delta k \end{pmatrix} + O(\delta k^3), \\ L(\delta k) &= \begin{pmatrix} 2(1-M) - \delta k & -\frac{i}{2}\delta k^2 \\ 2(1+i) - \frac{i}{2}\delta k^2 & -2M \end{pmatrix} + O(\delta k^3), \end{aligned} \quad (36)$$

and  $\det(R) \approx 2\delta k, \det(L) \approx -4M(1-M) + 2M\delta k$ , which gives us:

$$\det(h_0) = \det(R) \det(L) \approx -8M(1-M)\delta k. \quad (37)$$

Importantly, the fact that  $\det(R)$  is proportional to  $2\delta k$  and vanishes as  $\delta k \rightarrow 0$  will turn out to be crucial. According to Eq (35), for the first iteration,  $\det(h_0^{(1)})$ , can be calculated using  $R^{(1)}$  and  $L^{(1)}$

$$\begin{aligned} R^{(1)} &= \begin{pmatrix} R_{11} & R_{12} \\ R_{21} - (R^{-1})_{21} & R_{22} \end{pmatrix} = \begin{pmatrix} R_{11} & R_{12} \\ (1 + \frac{1}{\det(R)})R_{21} & R_{22} \end{pmatrix} \\ &\approx \begin{pmatrix} -\delta k & 2(1-i) + \frac{i}{2}\delta k^2 \\ \frac{i}{4}\delta k + \frac{i}{2}\delta k^2 & -2 - \delta k \end{pmatrix} + O(\delta k^3), \\ L^{(1)} &= \begin{pmatrix} L_{11} & L_{12} - (L^{-1})_{12} \\ L_{21} & L_{22} \end{pmatrix} = \begin{pmatrix} L_{11} & \left(1 - \frac{1}{4M(1-M)}\right)L_{12} \\ L_{21} & L_{22} \end{pmatrix} \\ &\approx \begin{pmatrix} 2(1-M) - \delta k & -\frac{i}{2}\left(1 - \frac{1}{4M(1-M)}\right)\delta k^2 \\ 2(1+i) - \frac{i}{2}\delta k^2 & -2M \end{pmatrix} \\ &+ O(\delta k^3), \end{aligned} \quad (38)$$

with  $\det(R^{(1)}) \approx (2 + \frac{1+i}{2})\delta k, \det(L^{(1)}) \approx -4M(1-M)$  and

$$\begin{aligned} \det(h_0^{(1)}) &= \det(R^{(1)}) \det(L^{(1)}) \\ &\approx -4M(1-M)\left(2 + \frac{1+i}{2}\right)\delta k. \end{aligned} \quad (39)$$

For the second and subsequent iterations ( $n \geq 2$ ), the elements  $R_{11/12/22}^{(n)}$  and  $L_{11/21/22}^{(n)}$  remain unchanged. And for

element  $[R^{(n)}]_{21}$ , we have

$$\begin{aligned} [R^{(2)}]_{21} &= R_{21} - [(R^{(1)})^{-1}]_{21} = R_{21} + \frac{R_{21}^{(1)}}{\det(R^{(1)})} \\ &\approx \frac{i}{10 + 2i} = \text{Const}, \\ \det(R^{(2)}) &\approx -\frac{1+i}{5+i} = \text{Const}, \\ [R^{(n)}]_{21} &= R_{21} - [(R^{(n-1)})^{-1}]_{21} = R_{21} + \frac{R_{21}^{(n-1)}}{\det(R^{(n-1)})} \\ &= \frac{i}{2}\delta k^2 + \frac{\text{Const}}{\text{Const}} \approx \text{Const}, \\ \det(R^{(n)})|_{n \geq 2} &\approx 2(1-i) * [R^{(n)}]_{21} = \text{Const}, \end{aligned} \quad (40)$$

and for  $[L^{(n)}]_{12}$ ,

$$\begin{aligned} [L^{(2)}]_{12} &= L_{12} - [(L^{(1)})^{-1}]_{12} = -\frac{i\delta k^2}{2} + \frac{L_{12}^{(1)}}{\det(L^{(1)})} \\ &\approx \frac{i\delta k^2}{2} \left( \frac{1}{4M(1-M)} - 1 \right), \\ \det(L^{(2)}) &\approx -4M(1-M) = \text{Const}, \\ [L^{(n)}]_{12} &= L_{12} + \frac{L_{12}^{(n-1)}}{\det(L^{(n-1)})} \sim \delta k^2, \\ \det(L^{(n)})|_{n \geq 2} &\approx -2(1-M) * 2M = -4M(1-M) \\ &= \text{Const}. \end{aligned} \quad (41)$$

Therefore, for  $n \geq 2$ , the determinant  $\det(h_0^{(n)})$  remains constant, leading to the quadratic dispersion:

$$\det(H_{\text{y-OBC}}) = \det(h_0) \det(h_0^{(1)}) \cdots \det(h_0^{(L_y-1)}) \sim \delta k^2. \quad (42)$$

- For most other generic parameter combinations, such as the case shown in Fig. 4(a), the constant term in  $\det(R)$  does not vanish i.e.,  $\det(R) \rightarrow \text{Const}$  as  $\delta k \rightarrow 0$ . Below we show how that leads to a qualitatively different dispersion. We have

$$\begin{aligned} \det(R) &\approx (f_0 + \delta)^2 - Z^2 - 2Z(f_0 + \delta - (1+i)\cos k_0)\delta k \\ &= C_0^R + C_1^R \delta k, \\ \det(L) &\approx (f_0 - \delta)^2 - Z^2 - 2Z(f_0 - \delta + (1-i)\cos k_0)\delta k \\ &= C_0^L + C_1^L \delta k, \\ \det(h_0) &= \det(R) \det(L) \\ &\approx C_0^R C_0^L + (C_0^R C_1^L + C_0^L C_1^R) \delta k. \end{aligned} \quad (43)$$

where  $C_0^{R(L)}$  and  $C_1^{R(L)}$  are constants. For the first itera-

tion, we have

$$\begin{aligned}
R^{(1)} &= \begin{pmatrix} R_{11} & R_{12} \\ R_{21} - (R^{-1})_{21} & R_{22} \end{pmatrix} \approx \begin{pmatrix} R_{11} & R_{12} \\ (1 + \frac{1}{C_0^R})R_{21} & R_{22} \end{pmatrix}, \\
\det(R^{(1)}) &\approx C_0^{(1)R} + C_1^{(1)R} \delta k, \\
L^{(1)} &= \begin{pmatrix} L_{11} & L_{12} - (L^{-1})_{12} \\ L_{21} & L_{22} \end{pmatrix} \approx \begin{pmatrix} L_{11} & (1 + \frac{1}{C_0^L})L_{12} \\ L_{21} & L_{22} \end{pmatrix}, \\
\det(L^{(1)}) &\approx C_0^{(1)L} + C_1^{(1)L} \delta k, \\
\det(h_0^{(1)}) &= \det(R^{(1)}) \det(L^{(1)}) \\
&\approx C_0^{(1)R} C_0^{(1)L} + (C_0^{(1)R} C_1^{(1)L} + C_0^{(1)L} C_1^{(1)R}) \delta k. \quad (44)
\end{aligned}$$

By analogy, for  $n \geq 2$ , we have

$$\begin{aligned}
[R^{(n)}]_{21} &= R_{21} - [(R^{(n-1)})^{-1}]_{21} = R_{21} + \frac{[R^{(n-1)}]_{21}}{\det(R^{(n-1)})} \\
&\sim R_{21}, \quad (45)
\end{aligned}$$

and similarly,  $[L^{(n)}]_{12} \sim L_{12}$ , which ensures that the expansion of  $\det(h_0^{(n)}) = \det(R^{(n)}) \det(L^{(n)}) \sim \det(h_0)$  always remains in the form of  $C_0^{(n)} + C_1^{(n)} \delta k$ . Therefore, in this case, we can obtain the linear dispersion of  $\det(H_{y\text{-OBC}})$  as:

$$\begin{aligned}
\det(H_{y\text{-OBC}}) &= \det(h_0) \det(h_0^{(1)}) \cdots \det(h_0^{(L_y-1)}) \\
&\approx (C_0 + C_1 \delta k) * (C_0^{(1)} + C_1^{(1)} \delta k) \cdots (C_0^{(L_y-1)} + C_1^{(L_y-1)} \delta k) \\
&\sim \delta k, \quad (46)
\end{aligned}$$

where the constant term  $C_0 C_0^{(1)} \cdots C_0^{(L_y-1)}$  goes to zero due to the existence of zero energy modes as shown in Fig. 4(a).

The above approach hinges on the observation that the two types of dispersion are distinguished by whether  $\det(R) = 0$ . It works for models where most matrix elements in  $h_+^y$  and  $h_-^y$  are 0, which effectively simplifies the calculation of  $h_0^{(n)} = h_0 - h_+ [h_0^{(n-1)}]^{-1} h_-$  in Eq (33). In more general models with hoppings beyond nearest neighbors, Eq (33) would need to be extended to handle multiple matrix diagonals, and this iterative approach could become far more complicated.

## B. Detailed analysis of the topological flat band model

In this section, we analyze the two-band model introduced in Eq. (9) of the main text

$$H(k, k_y) = t \cos k_y \sigma_x + (a_0 - t \sin k_y) \sigma_+ + ((b_0 - \cos k)^B + t \sin k_y) \sigma_-, \quad (47)$$

which possesses topological flat bands that experience the NHSE.

### 1. Exponential scaling of the topological gap with $L_y$ .

Here, we show that the topological gap  $\Delta$  of our flat band model exhibits exponential decay with respect to the system

size  $L_y$  within the topologically non-trivial regime. Considering OBCs in the  $y$ -direction, as similarly analyzed in the previous section, the Hamiltonian can be expressed as follows:

$$H_{y\text{-OBC}}(k) = \begin{pmatrix} h_0^y & h_+^y & \cdots & 0 & 0 \\ h_-^y & h_0^y & h_+^y & \cdots & 0 \\ 0 & h_-^y & h_0^y & \cdots & 0 \\ \vdots & \vdots & \ddots & \ddots & \vdots \\ 0 & 0 & \cdots & h_-^y & h_0^y \end{pmatrix}_{L_y \times L_y} \quad (48)$$

with

$$h_0^y = \begin{pmatrix} 0 & a_0 \\ (b_0 - \cos k)^B & 0 \end{pmatrix}, h_+^y = \begin{pmatrix} 0 & 0 \\ t & 0 \end{pmatrix}, h_-^y = \begin{pmatrix} 0 & t \\ 0 & 0 \end{pmatrix}. \quad (49)$$

Specifically, they satisfy the equation  $h_+^y (h_0^y)^{-1} h_-^y = 0$ . Therefore, for this model, we have

$$\begin{aligned}
\det(H_{y\text{-OBC}}(k)) &= \det(h_0^y) \det \begin{pmatrix} h_0^y & h_+^y & \cdots & 0 \\ h_-^y & h_0^y & \cdots & 0 \\ \vdots & \ddots & \ddots & \vdots \\ 0 & \cdots & h_-^y & h_0^y - h_+^y (h_0^y)^{-1} h_-^y \end{pmatrix} \\
&= \det(h_0^y) \det \begin{pmatrix} h_0^y & h_+^y & \cdots & 0 \\ h_-^y & h_0^y & \cdots & 0 \\ \vdots & \ddots & \ddots & \vdots \\ 0 & \cdots & h_-^y & h_0^y \end{pmatrix}_{(L_y-1) \times (L_y-1)} \\
&= (\det(h_0^y))^{L_y} = (a_0 (b_0 - \cos k)^B)^{L_y}. \quad (50)
\end{aligned}$$

To account for the NHSE experienced by system, we can perform a basis transform to the surrogate Hamiltonian [81]. Since  $H_{y\text{-OBC}}$  can be viewed as a non-Hermitian SSH model with  $k$ -dependent, asymmetric intra-cell hopping amplitudes  $a_0$  and  $b_0 - \cos k$ , Therefore, akin to the non-Hermitian SSH model [9], we can apply a similarity transformation to  $H_{y\text{-OBC}}$ ,

$$\begin{aligned}
H'(k) &= Q^{-1} H_{y\text{-OBC}}(k) Q, Q = \text{diag}\{1, r, r, r^2, \dots, r^{L_y-1}, r^{L_y-1}, r^{L_y}\}, \\
r &= \sqrt{\frac{(b_0 - \cos k)^B}{a_0}}, \quad (51)
\end{aligned}$$

and obtain a Hermitian matrix  $H'(k)$ :

$$H'(k) = \begin{pmatrix} 0 & t e^{-ik_y} + t' \\ t e^{ik_y} + t' & 0 \end{pmatrix}, \quad (52)$$

where  $t' = \sqrt{a_0 (b_0 - \cos k)^B}$ . Since a similarity matrix transform does not change the eigenspectrum,  $H'(k)$  possesses the same eigenvalues as  $H_{y\text{-OBC}}$ , with its bulk eigenvalues given by  $E_n = \pm \sqrt{(t e^{ik_y} + t')(t e^{-ik_y} + t')}$ . By substituting these values of  $E_n$  into  $\det[H_{y\text{-OBC}}(k)] = E_{e_1}(k) E_{e_2}(k) \prod_n E_n(k)$ , we obtain

$$\begin{aligned}
\prod_n E_n(k) &= - \prod_{k_y} (t e^{ik_y} + t')(t e^{-ik_y} + t') \\
&\sim t^{2L_y} + c_1 t^{2L_y-1} t' + c_2 t^{2L_y-2} t'^2 + \dots + c_{L_y} t'^{2L_y} \quad (53)
\end{aligned}$$

where in the RHS, the terms containing  $e^{\pm ik_y}$  are incorporated into the coefficients  $c_1, c_2, \dots, c_{L_y}$ . As mentioned in the main text, the topological non-trivial condition is  $|a_0(b_0 - \cos k)^B| \leq t^2$ , i.e.  $|t'| \leq |t|$ . Consequently, the leading term in the RHS of the above equation is  $t^{2L_y}$ . Then using Eq (53), we have

$$\begin{aligned}
\det[H_{y\text{-OBC}}(k)] &= E_{e_1}(k)E_{e_2}(k) * t^{2L_y} (1 + O(t'/t)) \\
&= (a_0(b_0 - \cos k)^B)^{L_y}. \\
E_{e_1}(k)E_{e_2}(k) &\approx \frac{(a_0(b_0 - \cos k)^B)^{L_y}}{t^{2L_y}}. \tag{54}
\end{aligned}$$

And because  $E_{e_1} = -E_{e_2}$ , we ultimately obtain the scaling of topological gap  $\Delta$  with  $L_y$  as follows:

$$\Delta = 2|E_{e_1}| \sim \left( \frac{a_0(b_0 - \cos k)^B}{t^2} \right)^{L_y/2}. \quad (55)$$

## 2. Scaling of entanglement entropy $S_A$ with system sizes $L$ and $L_y$ in the case of gapless flat bands

In this subsection, we derive the scaling relations of  $S_A$  as a function of  $L_y$  and  $L$ , specifically Eq (13) in the main text:

$$S_A \sim -\frac{1}{2}(BL_y)^2 \log L \quad (56)$$

for the gapless case of  $b_0 = 1$ . This is a highly unusual scaling behavior because  $S_A$  scales faster than  $L_y$ , the number of states (volume) from the  $y$ -dimension. Below we shall elucidate the origin of this super volume-law entanglement scaling behavior. While it may naively appear that this extra factor of  $BL_y$  scaling (quadratic vs. linear i.e. volume-law) originates from the high-order topological flat band dispersion  $E(k) \sim k^{BL_y}$ , below we shall show that the full story is more complicated, crucially involving the NHSE.

To establish the scaling relation of  $S_A$ , we first need to prove that:

$$\text{Tr}(\bar{P}^2) = \sum_i p_i^2 \sim c_1 L^{BL_y-1} + c_2 L^{BL_y-1-2} + \dots, \quad (57)$$

where  $p_i$  represents the eigenvalues of  $\bar{P}$ , and  $c_1, c_2, \dots$  are coefficients that are independent of  $L$ . In other words, that the eigenvalues  $p_i$  of  $\bar{P}$  scales like various powers of  $L$ , up to  $L^{BL_y-1}$ .

Below, we present a comprehensive derivation of Eq (57). Under OBCs in the  $y$  direction,  $k$  is still a good eigenstate label and the projector operator in  $k$  space is defined as  $P(k) = \sum_{n \in \text{occ}} |\psi_n(k)^R\rangle \langle \psi_n(k)^L|$ . Due to the NHSE which pushes all right eigenstates in the  $y$ -direction towards the same edge, they become highly edge-localized and hence almost orthogonal. This large overlap ensures that the corresponding left edge eigenstates exhibit large amplitudes and contribute most significantly to  $P(k)$ . Therefore,  $P(k)$  is dominated by the edge state contributions:

$$\begin{aligned}
 P(k) &= \sum_{n \in occ} |\psi_n(k)^R\rangle \langle \psi_n(k)^L| \\
 &\approx |\psi_{edge}(k)^R\rangle \langle \psi_{edge}(k)^L| = P_{edge}(k).
 \end{aligned} \tag{58}$$

In the following discussion, for the sake of brevity, we will omit the  $k$  in  $|\psi_{edge}(k)^R\rangle, \langle\psi_{edge}(k)^L|$ , rewriting them as  $|\psi_{edge}^R\rangle, \langle\psi_{edge}^L|$ . To proceed, we note that  $P_{edge}(k)$  is furthermore dominated by just *one* matrix element due to the exponential skin-localization of the edge states. To show this explicitly, we use the similarity transform [Eq (52)] to write the spatial profiles of the topological SSH edge states in the  $y$  direction as

$$|\psi'_{edge}(y)\rangle = \begin{pmatrix} \psi'^A(y) \\ \psi'^B(y) \end{pmatrix} \sim \begin{pmatrix} e^{y-1} \\ e^{L_y-y} \end{pmatrix},$$

$$\text{re } \epsilon = \left| \frac{t'}{t} \right| = \sqrt{\frac{a_0}{t} (b_0 - \cos k)^B}. \quad (59)$$

Consequently, the right and left edge states of the original  $H_y$ -OBC is given by

$$|\psi_{edge}^R\rangle = Q|\psi_{edge}'\rangle \sim \begin{pmatrix} 1 \\ r\epsilon^{L_y-1} \\ r\begin{pmatrix} \epsilon \\ r\epsilon^{L_y-2} \end{pmatrix} \\ \vdots \\ r^{L_y-2}\begin{pmatrix} \epsilon^{L_y-2} \\ r\epsilon \end{pmatrix} \\ r^{L_y-1}\begin{pmatrix} \epsilon^{L_y-1} \\ r \end{pmatrix} \end{pmatrix}, \quad (60)$$

and

$$\langle \psi_{edge}^L \rangle = Q^{-1} \langle \psi'_{edge} \rangle \sim \begin{pmatrix} 1 \\ \epsilon^{L_y-1}/r \\ \frac{1}{r} \begin{pmatrix} \epsilon \\ \epsilon^{L_y-2}/r \end{pmatrix} \\ \vdots \\ \frac{1}{r^{L_y-2}} \begin{pmatrix} \epsilon^{L_y-2} \\ \epsilon/r \end{pmatrix} \\ \frac{1}{r^{L_y-1}} \begin{pmatrix} \epsilon^{L_y-1} \\ 1/r \end{pmatrix} \end{pmatrix} . \quad (61)$$

This yields the following form for the projector matrix

$$P(k) \approx P_{\text{edge}}(k) = |\psi_{\text{edge}}^R\rangle \langle \psi_{\text{edge}}^L|$$

$$= \begin{pmatrix} \left( \begin{matrix} 1 & e^{Ly-1}/r \\ re^{Ly-1} & e^{2Ly-2}/r \end{matrix} \right) & \left( \begin{matrix} e & e^{Ly-2}/r \\ re^{Ly-1} & e^{2Ly-3} \end{matrix} \right) & \cdots & \left( \begin{matrix} 1 & e^{Ly-1}/r \\ re^{2Ly-2} & e^{Ly-1} \end{matrix} \right) \\ \left( \begin{matrix} e & e^{Ly}/r \\ re^{Ly-2} & e^{Ly-2} \end{matrix} \right) & \left( \begin{matrix} e^2 & e^{Ly-1}/r \\ re^{Ly-1} & e^{2Ly-4} \end{matrix} \right) & \cdots & \left( \begin{matrix} 1 & e^{Ly}/r \\ re^{2Ly-3} & e^{Ly-2} \end{matrix} \right) \\ \vdots & \vdots & \vdots & \vdots \\ \left( \begin{matrix} e^{Ly-1} & e^{2Ly-2}/r \\ r & e^{Ly-1} \end{matrix} \right) & \left( \begin{matrix} e^{Ly} & e^{2Ly-3}/r \\ re & e^{Ly-2} \end{matrix} \right) & \cdots & \left( \begin{matrix} e^{2Ly-2} & e^{Ly-1}/r \\ re^{Ly-1} & 1 \end{matrix} \right) \end{pmatrix}_{2Ly \times 2Ly} \quad (62)$$

which is dominated by the upper right matrix element in blue, since  $r = \sqrt{\frac{(b_0 - \cos k)^2}{a_0}} < 1$  for the parameters used.

The truncated projector  $\bar{P}$  can be obtained by Fourier transforming each matrix element on the right-hand side (RHS) of Eq (62), i.e.,

$$\bar{P} = \begin{pmatrix} \bar{P}_{1,1} & \bar{P}_{1,2} & \cdots & \bar{P}_{1,2L_y} \\ \bar{P}_{2,1} & \bar{P}_{2,2} & \cdots & \bar{P}_{2,2L_y} \\ \vdots & \vdots & \ddots & \vdots \\ \bar{P}_{2L_{\text{sc}},1} & \bar{P}_{2L_{\text{sc}},2} & \cdots & \bar{P}_{2L_{\text{sc}},2L_{\text{sc}}} \end{pmatrix}, \quad (63)$$

where  $\bar{P}_{m,n}$  is an  $l \times l$  matrix whose elements are

$$\langle x_1 | \bar{P}_{m,n} | x_2 \rangle = \frac{1}{L} \sum_k e^{ik(x_1-x_2)} P_{m,n}(k), \quad (64)$$

with  $l$  denoting the size of subregion  $A$  and  $x_1, x_2 \in A$ . The dominant submatrix  $\bar{P}_{1,2L_y}(k)$  is, after Fourier transformation into real space and substituting  $r = \sqrt{\frac{(b_0-\cos k)^B}{a_0}}$ , given by

$$\begin{aligned} \langle x_1 | \bar{P}_{1,2L_y} | x_2 \rangle &= \frac{1}{L} \sum_k e^{ik(x_1-x_2)} P_{1,2L_y}(k) \\ &\sim \frac{1}{L} a_0^{L_y/2} \frac{2 \cos(k_1(x_1-x_2))}{(b_0 - \cos k_1)^{BL_y/2}} \\ &\sim a_0^{L_y/2} \left( \frac{L}{\pi} \right)^{BL_y-1} \times \left( 1 - \frac{1}{2} \left( \frac{\pi x}{L} \right)^2 + \frac{1}{4!} \left( \frac{\pi x}{L} \right)^4 - \frac{1}{6!} \left( \frac{\pi x}{L} \right)^6 + \dots \right) \\ &= c_1 L^{BL_y-1} + c_2 L^{BL_y-1-2} + \dots, \end{aligned} \quad (65)$$

with  $b_0 = 1$  and the leading  $k = \pm k_1 = \pm \pi/L$  contributions substituted to obtain the 3rd line. The other matrix elements scale more slowly with  $L$ . Since  $\langle x_1 | \bar{P}_{2L_y,1} | x_2 \rangle \sim O(1)$ , we have established Eq (57):

$$\text{Tr}(\bar{P}^2) \approx 2\text{Tr}(\bar{P}_{1,2L_y} \bar{P}_{2L_y,1}) \sim c_1 L^{BL_y-1} + c_2 L^{BL_y-1-2} + \dots \quad (66)$$

where, as a first-order approximation, we have retained only the term containing the largest block  $P_{1,2L_y}$  and disregarded the contributions from other elements. This implies that the eigenvalues  $p_i$  generically scale like  $p_i \sim cL^\alpha$  with  $c$  an unimportant constant. For odd  $BL_y$ ,  $\alpha = 1, 2, \dots, (BL_y-1)/2$  and for even  $BL_y$ ,  $\alpha = 1/2, 3/2, \dots, (BL_y-1)/2$ .

For each  $p_i = cL^\alpha$  ( $c$  is a constant), its contribution to entanglement entropy  $S_A$  is

$$\begin{aligned} S_A(p_i) &= -p_i \log p_i - (1 - p_i) \log(1 - p_i) \\ &= -cL^\alpha \log(cL^\alpha) - (1 - cL^\alpha) \log(1 - cL^\alpha) \\ &= -cL^\alpha \log(cL^\alpha) + cL^\alpha \log(1 - cL^\alpha) - \log(1 - cL^\alpha) \\ &\approx -cL^\alpha \log(cL^\alpha) + cL^\alpha \log(-cL^\alpha) - \log(1 - cL^\alpha) \\ &= (cL^\alpha + 1) \log(-1) - \log(cL^\alpha) \\ &\approx -\alpha \log L + cL^\alpha \pi i - \log c. \end{aligned} \quad (67)$$

The other eigenvalue with  $p'_i = 1 - p_i$  (see subsection C.2) contributes the same real part to  $S_A$ , but opposite imaginary part that cancels off, as numerically observed as twofold degenerate states. Therefore, the total entanglement entropy is dominated by the  $\log L$  contribution in blue above which should be multiplied by 4, i.e.,

$$\begin{aligned} S_A &= \sum_{p_i} -p_i \log p_i - (1 - p_i) \log(1 - p_i) \\ &\sim -4 \times \left[ \frac{BL_y-1}{2} + \left( \frac{BL_y-1}{2} - 1 \right) + \left( \frac{BL_y-1}{2} - 2 \right) + \dots \right] \log L. \end{aligned} \quad (68)$$

Calling  $J = \frac{BL_y-1}{2}$  ( $B, L_y \in \mathbb{Z}$ ) and  $J' = \lceil J \rceil = \begin{cases} J, & BL_y \text{ is odd} \\ J + 1/2, & BL_y \text{ is even} \end{cases}$ , we finally obtain the scaling relation

of  $S_A$  with  $L, L_y$  as

$$\begin{aligned} S_A &\sim -4 \log L (J + (J-1) + (J-2) + \dots + (J-J'+1)) \\ &= -2J'(2J-J'+1) \log L \\ &= -\frac{1}{2} ((BL_y)^2 - (BL_y \bmod 2)) \log L \\ &= -\left\lceil \frac{B^2 L_y^2 - 1}{2} \right\rceil \log L \sim -\frac{1}{2} (BL_y)^2 \log L, \end{aligned} \quad (69)$$

which is our key super volume-law negative entanglement scaling result.

Below, we further present the numerical verification of Eq (68). In Fig. 7(a), we take  $L_y = 3, B = 1$ , since  $\frac{BL_y-1}{2} = 1$ , only the first order  $p_i \sim L^1$  exists. The numerical fitting shown in Fig. 7(d) yields:

$$S_A \sim -4.4072 \log L \approx -4 \times \frac{BL_y-1}{2} \log L = -4 \log L, \quad (70)$$

which demonstrates good agreement with Eq (68). In Fig. 7(b), where  $L_y = 5, B = 1$ ,  $\frac{BL_y-1}{2} = 2$ , both the first and second orders of  $L$  in  $p_i \sim L^1, p_i \sim L^2$  are present. We numerically obtain the scaling of entanglement entropy as depicted in Fig. 7(e):

$$\begin{aligned} S_A &\sim -11.7648 \log L \\ &\approx -4 \times \left( \frac{BL_y-1}{2} + \frac{BL_y-1}{2} - 1 \right) \log L = -12 \log L \end{aligned} \quad (71)$$

For the case of  $L_y = 3, B = 2$  shown in Fig. 7(c), the first, second and third orders of  $L$  all contribute to the EE:

$$\begin{aligned} S_A &\sim -17.1980 \log L \\ &\approx -4 \times \left( \frac{BL_y-1}{2} + \frac{BL_y-1}{2} - 1 + \frac{BL_y-1}{2} - 2 \right) \log L \\ &= -18 \log L. \end{aligned} \quad (72)$$

While plots with even larger  $L_y$  and  $B$  would be more prone to numerical errors due to the larger  $L$  needed, excellent agreement is already observed for these cases which corresponds to the most realistic models.

### 3. Scaling of entanglement entropy $S_A$ for gapped flat bands

In the case of gapped bands where  $b_0 > 1$  (e.g.,  $b_0 = 1.2$ ), there exists a small gap  $\Delta$  in the topological flat edge bands. Due to this gap, the entanglement entropy  $S_A$  decreases with increasing system size  $L$  and eventually stabilizes at a minimum constant value,  $S_{\min}$ . In this section, we will demonstrate that:

- 1) For  $L \ll L_y$ ,  $S_A$  exhibits an approximate negative  $L_y$ -linear scaling with  $\log L$ , expressed as  $S_A \sim -(\alpha L_y + \beta) \log L$ , where  $\alpha$  and  $\beta$  are fitting coefficients with  $\alpha > 0$ ;
- 2) While for  $L \gg L_y$ ,  $S_A$  saturates to the lower bound,  $S_{\min}$ , which scales linearly with  $L_y$  as:  $S_{\min} \sim -L_y \log \left( \frac{a_0}{(b_0-1)^B} \right)$ .

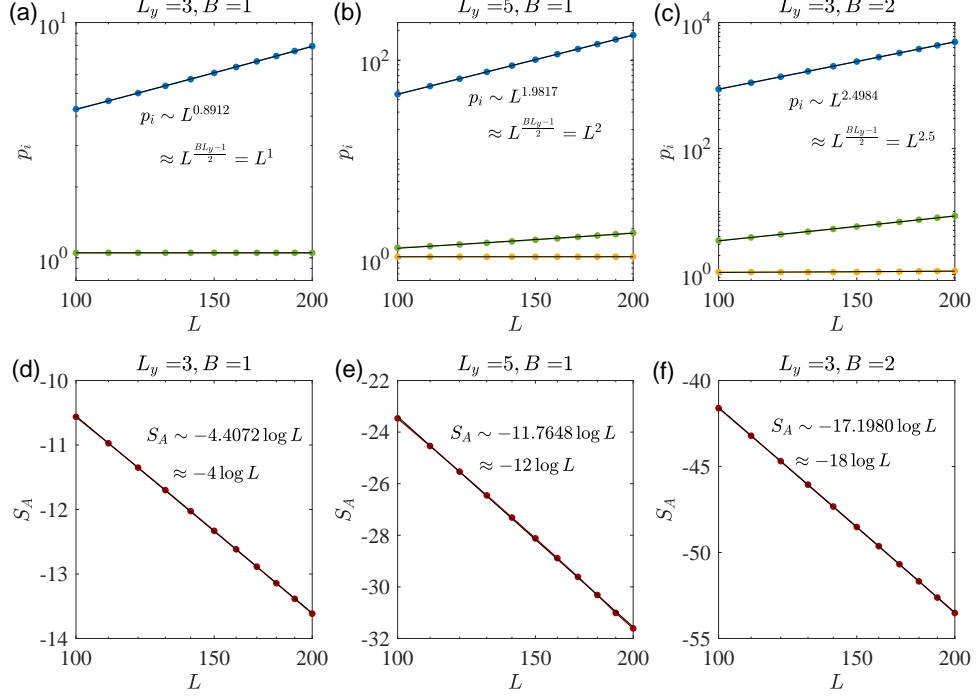


FIG. 7. Excellent agreement of our super-volume-law negative entanglement scaling result with numerics for various  $B$  and  $L_y$ , both for the  $\tilde{P}$  eigenvalues  $p_i$  [Eq (57)] (a-c) and the corresponding entanglement scaling  $S_A \sim -[(B^2 L_y^2 - 1)/2] \log L$  [Eq (69)]. Parameters:  $t = 0.5, a_0 = 2, b_0 = 1$ .

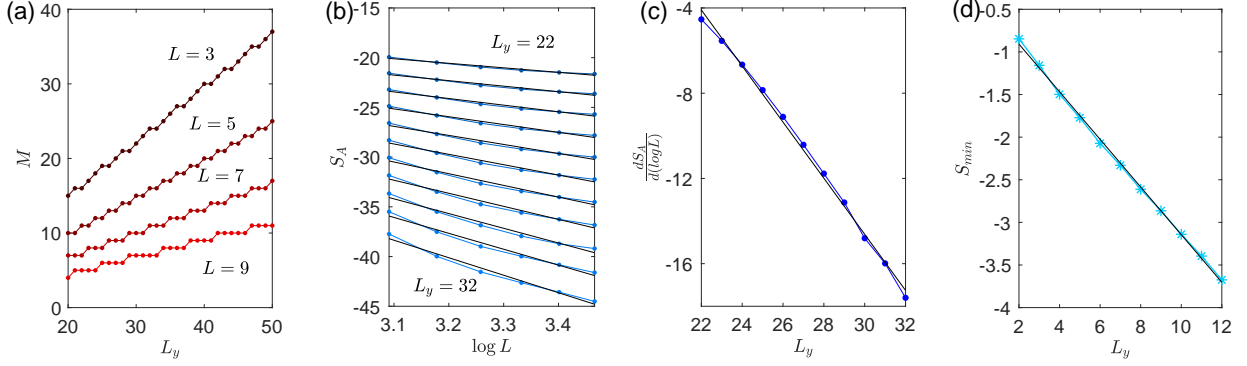


FIG. 8. Negative entanglement scaling for the gapped EP case ( $b_0 > 1$ ). (a) As numerically plotted for  $L = 9, b_0 = 1.2$ , the approximate linear scaling of the scaling exponent  $M$  of the dominant  $\tilde{P}$  eigenvalue with  $L_y$ , as described by Eq (75). (b) The negatively linear relationship of the entanglement entropy  $S_A$  with  $\log L$  for different  $L_y$  ranging from 22 to 32, with  $L \in [22, 32]$  and parameters  $t = 0.8, a_0 = 1, b_0 = 1.2, B = 1$ . As predicted in Eq (78), the gradient indeed increases with  $L_y$ . (c) Using the same parameters as in (b), approximate linear dependence of the gradient of  $S_A$  on  $L_y$ . (d) For large  $L = 60$  and parameters  $t = 0.8, B = 1, b_0 = 1.2, a_0 = 2, S_{\min}$  indeed scales linearly with  $L_y$ , as predicted in Eq (81).

As discussed in subsection B.2, we demonstrated that near  $k = 0$ , the dominant element of  $P(k)$  is located in the upper right corner, where  $P_{1,2L_y}(k) \sim 1/r^{L_y}$  with  $r = \sqrt{\left|\frac{(b_0 - \cos k)^B}{a_0}\right|} < 1$ . For  $b_0 > 1$ , this can still be the case with appropriate choice

of  $a_0$ . We have

$$\begin{aligned} \langle x_1 | \tilde{P}_{1,2L_y} | x_2 \rangle &= \frac{1}{L} \sum_k e^{ik(x_1 - x_2)} P_{1,2L_y}(k) \\ &\sim \frac{1}{L} \sum_k e^{ik(x_1 - x_2)} a_0^{L_y/2} \frac{1}{(b_0 - \cos k)^{BL_y/2}} \end{aligned} \quad (73)$$

where  $k$  takes the values  $\pi/L, 3\pi/L, 5\pi/L, \dots$ . For  $k_1 = \pi/L$ ,

which contributes most significantly to  $\langle x_1 | \bar{P}_{1,2L_y} | x_2 \rangle$ , we have

$$(b_0 - \cos k_1)^{BL_y/2} = (b_0 - 1 + 1 - \cos k_1)^{BL_y/2} = (b_0 - 1)^{BL_y/2}(1 + x)^{BL_y/2}, \quad (74)$$

where  $x = \frac{1-\cos k_1}{b_0-1} \approx \frac{\pi^2}{2(b_0-1)L^2}$ .

When  $L \ll L_y$ , (for simplicity, we select  $L_y$  to be an even number to ensure  $BL_y/2$  is an integer), the following approximation holds

$$(1 + x)^{BL_y} = \sum_m C_{BL_y/2}^m x^m \approx C_{BL_y/2}^M x^M \quad (75)$$

where  $m = M$  represents the maximum term in the summation. As verified in Fig. 8(a),  $M$  exhibits a linear relation with  $L_y$ , expressed as  $M \approx \frac{1}{2}(\gamma L_y + \zeta)$  (where  $\gamma, \zeta$  are coefficients independent of  $L_y$ ). Consequently, we find

$$(1 + x)^{BL_y} \approx C_{BL_y/2}^M x^M \sim C_{BL_y/2}^{(\gamma L_y + \zeta)/2} \left( \frac{\pi^2}{2(b_0 - 1)L^2} \right)^{(\gamma L_y + \zeta)/2} \sim L^{-(\gamma L_y + \zeta)}. \quad (76)$$

By substituting into Eqs (74) and (73) and considering only the contribution from  $k_1 = \pi/L$ , we have

$$\langle x_1 | \bar{P}_{1,2L_y} | x_2 \rangle \sim \frac{1}{L} e^{ik_0(x_1-x_2)} \frac{a_0^{L_y/2}}{(b_0 - 1)^{BL_y/2}(1 + x)^{BL_y/2}} \sim L^{\gamma L_y + \zeta - 1}. \quad (77)$$

As we have demonstrated in the previous subsection B.2, since the elements of  $\bar{P}_{1,2L_y}$  are proportional to  $L^{\gamma L_y + \zeta - 1}$ , we can deduce:

$$\begin{aligned} \text{Tr}(\bar{P}^2) &\approx 2\text{Tr}(\bar{P}_{1,2L_y} \bar{P}_{2L_y,1}) \sim L^{\gamma L_y + \zeta - 1} \\ \implies p_i^{1st} &\sim L^{\frac{\gamma L_y + \zeta - 1}{2}}, \\ S_A &\sim -4 \times \left( \frac{\gamma L_y + \zeta - 1}{2} \right) \log L \\ &\sim -(\alpha L_y + \beta) \log L, \end{aligned} \quad (78)$$

where we have redefined  $2\gamma$  as  $\alpha$  and  $2(\zeta - 1)$  as  $\beta$ . In the  $L \ll L_y$  regime, higher orders of  $p_i$  are negligible, and we only need to consider the first order. Therefore, we conclude: for  $L \ll L_y$ ,  $S_A \sim -\log L$  (Fig. 8(b)), with the gradient depending linearly on  $L_y$  (see Fig. 8(c)). Even though our derivation had assumed  $L \ll L_y$ , from the numerics in Fig. 1(e) of the main text, we see that this trend still mostly holds as long as  $L < L_y$ .

When  $L \gg L_y$ , Eq (74) can be approximated as:

$$\begin{aligned} (b_0 - \cos k_0)^{BL_y/2} &= \left( b_0 - 1 + \frac{1}{2!} \left( \frac{\pi}{L} \right)^2 - \frac{1}{4!} \left( \frac{\pi}{L} \right)^4 + \dots \right)^{BL_y/2} \\ &\approx (b_0 - 1)^{BL_y/2}. \end{aligned} \quad (79)$$

Thus, Eq (73), which represents the elements of the largest matrix block  $\bar{P}_{1,2L_y}$ , can be expressed as

$$\langle x_1 | \bar{P}_{1,2L_y} | x_2 \rangle \sim \left( \frac{a_0}{(b_0 - 1)^B} \right)^{L_y/2}. \quad (80)$$

Following a similar derivation as Eq (78), we now have

$$\begin{aligned} \text{Tr}(\bar{P}^2) &\sim \left( \frac{a_0}{(b_0 - 1)^B} \right)^{L_y/2}, \quad p_i^{1st} \sim \left( \frac{a_0}{(b_0 - 1)^B} \right)^{L_y/4} \\ S_{min} &\sim -4 \times \frac{L_y}{4} \log \left( \frac{a_0}{(b_0 - 1)^B} \right) \\ &= -L_y \log \left( \frac{a_0}{(b_0 - 1)^B} \right). \end{aligned} \quad (81)$$

This linear dependence on  $L_y$  is verified in Fig. 8(d). Empirically, we also see from Fig. 1(e) of the main text that this saturation generally sets in as long as  $L$  exceeds  $L_y$ .

### C. Further properties of the negative entanglement

#### 1. Complex $p_i$ and the negativity of von Neumann and Rényi entropy

In general non-Hermitian systems, the eigenvalues  $p_i$  of  $\bar{P}$  are complex, making it unintuitive in determining how  $p_i$  affects the real part of  $S_A$ . In this section, we discuss this issue in detail. Most importantly, we will demonstrate that the negativity in entanglement is not only limited to the von Neumann entropy, but also can be extended to nth-order ( $n \geq 2$ ) Rényi entropies.

First, for the von Neumann entropy, we consider a general complex eigenvalue  $p_i = |p_i|e^{i\theta}$ , analyzing two cases:  $|p_i| \in [0, 1]$  and  $|p_i| \gg 1$ . As shown in Fig. 9(a), for  $|p_i| \in [0, 1]$ ,  $\text{Re}(S_A)$  becomes negative near  $\theta = \pi$ , where  $\text{Re}(p_i) < 0$  and  $\text{Im}(p_i)$  is approximately zero. For the case of  $|p_i| \gg 1$ , the negative contribution occurs more sharply around  $\theta = 0, \pi$  (see the inset of Fig. 9(b)), where  $\text{Re}(p_i)$  is either much less than 0 or greater than 1, while  $\text{Im}(p_i)$  remains negligible.

Thus, for the von Neumann entropy, we conclude that for nearly real  $p_i$ , when  $\text{Re}(p_i) > 1$  or  $\text{Re}(p_i) < 0$ , it contributes negatively to  $\text{Re}(S_A)$ . This conclusion can also be derived as follows:

$$\begin{aligned} \text{Re}[S_A(p_i)] &= \text{Re}[-p_i \log(p_i) - (1 - p_i) \log(1 - p_i)] \\ &= \begin{cases} -p_i \log(p_i) + (p_i - 1) \log(p_i - 1) < 0, \text{ real } p_i > 1 \\ |p_i| \log(|p_i|) - (|p_i| + 1) \log(|p_i| + 1) < 0, \text{ real } p_i < 0 \end{cases} \end{aligned} \quad (82)$$

Since the above discussion is based on the condition that  $p_i$  is nearly real, we numerically calculated the values of  $p_i$  for the two models introduced in our paper. As shown in Figs. 10(c) and (f), we focus primarily on the  $p_i$  values whose real parts extend beyond the range  $[0, 1]$  (as highlighted by the circles in Figs. 10(b) and (e)). We observe that  $\text{Im}(p_i)$  remains close to zero, indicating that it is indeed negligible compared to  $\text{Re}(p_i)$ . As expected, these  $p_i$  contribute to a negative scaling of  $\text{Re}(S_A)$  for both models, as shown in Figs. 10(a) and (d).

Secondly, we derive how the complex  $p_i$  contributes to the real part the  $n$ -th order Rényi entropy. For the case  $|p_i| \gg 1$ , which, as demonstrated in the main article, is induced by the

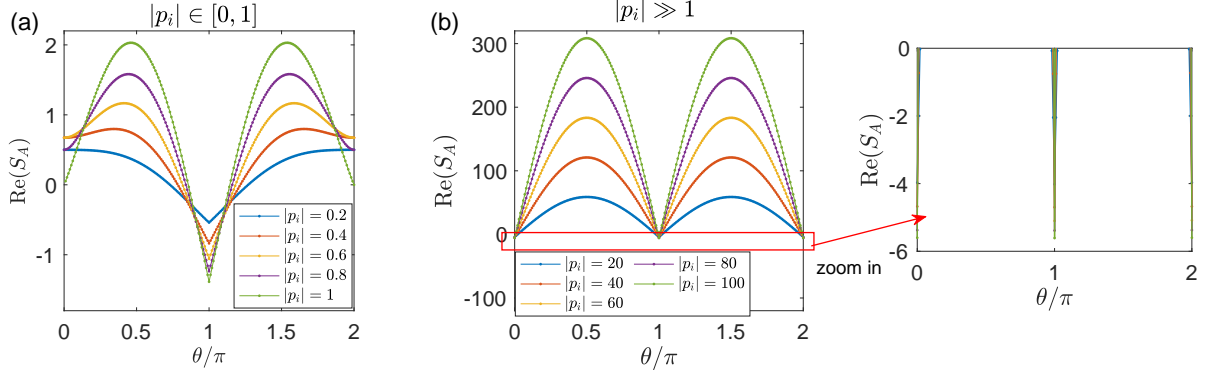


FIG. 9. Contribution of a complex  $p_i = |p_i|e^{i\theta}$  to the real part of  $S_A$  for two cases: (a)  $|p_i| \in [0, 1]$  and (b)  $|p_i| \gg 1$ .

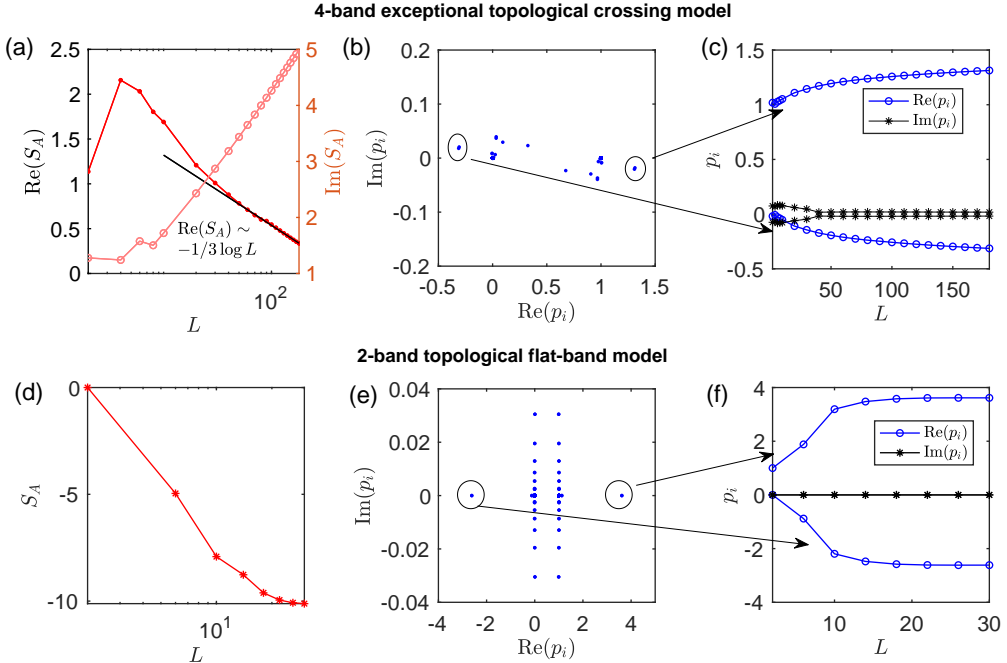


FIG. 10. Negligible imaginary part for complex  $p_i$  with  $\text{Re}(p_i) > 1$  or  $\text{Re}(p_i) < 0$  in both the 4-band exceptional crossing model (a-c) and the 2-band topological flat-band model (d-f). (a) Replot of the topo, non-Hermitian case from Fig. 1(d). (c) Corresponding scaling of  $\text{Re}(p_i)$  and  $\text{Im}(p_i)$  for the complex  $p_i$  circled in (b). (d) Replot of the  $L_y = 15$  case from Fig. 2(e). (f) Corresponding scaling of  $\text{Re}(p_i)$  and  $\text{Im}(p_i)$  for the complex  $p_i$  circled in (e).

large overlap of different eigenstates, we have:

$$p_i^n + (1 - p_i)^n \sim \begin{cases} p_i^n + O(p_i^{n-1}), & \text{for even } n \\ p_i^{n-1} + O(p_i^{n-2}), & \text{for odd } n \end{cases} \quad (83)$$

Thus, considering only the dominant term, we approximately have:

$$\begin{aligned} S_A^{(n)}(p_i) &= \frac{1}{1-n} \log(p_i^n + (1 - p_i)^n) \\ &\sim \begin{cases} \frac{n}{1-n} (\log |p_i| + i \arg(p_i)), & \text{for even } n \\ -(\log |p_i| + i \arg(p_i)), & \text{for odd } n \end{cases}, \\ \text{Re}[S_A^{(n)}(p_i)] &\sim \begin{cases} \frac{n}{1-n} \log |p_i|, & \text{for even } n \\ -\log |p_i|, & \text{for odd } n \end{cases} < 0. \end{aligned} \quad (84)$$

Hence, unlike the von Neumann entropy, for general complex  $p_i$  with  $|p_i| \gg 1$ , even if the imaginary part is not negligible, its contribution to the real part of Rényi entropy is always negative.

## 2. *PT*-symmetry-protected real entanglement entropy $S_A$ in the flat band model.

In this section, we demonstrate that both the von Neumann entropy and Rényi entropies are rigorously real for *PT*-symmetry-protected models, as exemplified by our topological flat band model. This result arises from the fact that the eigenvalues  $p_i$  of  $\bar{P}$  consistently occur in complex conjugate

pairs.

First, in the  $H_y$ -OBC( $k$ ) model of Eq (49), the parameters  $a_0, b_0, t$  are always real numbers, with  $b_0 \geq 1$ . As previously demonstrated, this model can be viewed as a non-Hermitian SSH model that is protected by PT-symmetry, and it features purely real eigenvalues and eigenvectors,  $|\psi_n^R(k)\rangle$  and  $\langle\psi_n^L(k)|$ . Therefore, the elements of the projector matrix  $P_{\alpha,\beta}(k) = \sum_{n \in \text{occ}} \langle\alpha|\psi_n^R(k)\rangle\langle\psi_n^L(k)|\beta\rangle$  are all real, with  $\alpha, \beta$  labeling the band indices. Upon expanding these elements into real space, and given that  $P_{\alpha,\beta}(k)$  are real, we will obtain

$$\langle x_1|P_{\alpha,\beta}|x_2\rangle = \sum_k P_{\alpha,\beta}(k) e^{ik(x_1-x_2)} = \left(\langle x_2|P_{\alpha,\beta}|x_1\rangle\right)^*. \quad (85)$$

Hence, the real-space truncated projector  $\bar{P}$  satisfy

$$V\bar{P}V^{-1} = \text{conj}(\bar{P}), \text{ with } V = \begin{pmatrix} 0 & 0 & 0 & \cdots & \mathbb{I} \\ 0 & 0 & \cdots & \mathbb{I} & 0 \\ 0 & \cdots & \mathbb{I} & 0 & 0 \\ \vdots & \vdots & \vdots & \vdots & \vdots \\ \mathbb{I} & 0 & 0 & \cdots & 0 \end{pmatrix}, \quad (86)$$

indicating that  $\bar{P}$  possesses PT-symmetry and its spectrum must consists of complex conjugate pairs  $(p, p^*)$ .

For the conjugate pairs  $(p, p^*) = (|p|e^{i\theta}, |p|e^{-i\theta})$ , their contribution to the von Neumann entropy is:

$$\begin{aligned} S_A^{\text{pair}} &= -|p|e^{i\theta} \log(|p|e^{i\theta}) - (1 - |p|e^{i\theta}) \log(1 - |p|e^{i\theta}) \\ &\quad -|p|e^{-i\theta} \log(|p|e^{-i\theta}) - (1 - |p|e^{-i\theta}) \log(1 - |p|e^{-i\theta}) \\ &= 2|p|(\theta \sin \theta - \log |p| \cos \theta) + 2|p'|(θ' \sin θ' - \log |p'| \cos θ'), \end{aligned} \quad (87)$$

where  $|p'|, \theta'$  are defined such that  $1 - |p|e^{i\theta} = |p'|e^{i\theta'}$ . As shown above,  $\text{Im}(S_{\text{pair}}) = 0$ , indicating that the von Neumann entropy should be a purely real. And their contribution to the  $n$ -th order Rényi entropy is:

$$\begin{aligned} (S_A^{(n)})^{\text{pair}} &= \frac{\log [p^n + (1 - p)^n]}{1 - n} + \frac{\log [(p^*)^n + (1 - p^*)^n]}{1 - n} \\ &= \frac{1}{1 - n} \log (|p''|e^{i\theta''}) + \frac{1}{1 - n} \log (|p''|e^{-i\theta''}) \\ &= \frac{2}{1 - n} \log |p''|, \end{aligned} \quad (88)$$

where we have defined

$$p^n + (1 - p)^n = |p''|e^{i\theta''}. \quad (89)$$

This result shows that  $\text{Im}[(S_A^{(n)})^{\text{pair}}] = 0$ , i.e., the Rényi entropies are purely real. Therefore, any observed imaginary part of the entanglement entropy in numerical computations must be attributed to numerical errors.

### 3. Further discussion on the role of $\bar{P}$ eigenvalues.

In many-body free fermion systems, as discussed in this paper, the von Neumann entropy (or Rényi entropy) is a mathematical function of the eigenvalues  $p_i$  of the truncated projector operator  $\bar{P}$ . This highlights that the truncated projector operator itself can be regarded as a more fundamental quantity, encapsulating the essential features of the system's entanglement structure.

As highlighted in previous studies [35], the presence of significant coalescence between the right eigenstates causes the momentum-space projector  $P(k)$  to approach singularity. When transformed into real space, this results in the projector operators  $P$  and  $\bar{P}$  exhibiting slowly decaying, long-range matrix hopping elements. In contrast, in trivial cases with no substantial overlap,  $\bar{P}$  is characterized by short-range matrix hopping elements. A striking consequence of these long-range matrix hopping elements is the emergence of unique eigenmodes, referred to as Exceptional Bound States. These modes are distinguished by the real parts of their eigenvalues extending well beyond the typical range of  $[0, 1]$ , ultimately contributing to a negative real component of the entanglement entropy (EE). Thus, the emergence of these modes represents a fundamental and profound consequence of the large overlap.

Hence, even without focusing on the entanglement entropy, the presence of a large eigenstate overlap can be regarded as a physical phenomenon in itself if the  $\bar{P}$  matrix elements are taken to be physical hoppings. For instance, by constructing a long-range hopping system i.e. a circuit metamaterial array and designing the Hamiltonian to mimic the topologically protected, non-trivial  $\bar{P}$  introduced in this paper, one would observe a novel energy spectrum. This spectrum features special isolated eigenenergies that lie well outside the conventional range of  $[0, 1]$ .

---

[1] D. Gioev and I. Klich, Entanglement entropy of fermions in any dimension and the widom conjecture, *Phys. Rev. Lett.* **96**, 100503 (2006).

[2] S. T. Flammia, A. Hamma, T. L. Hughes, and X.-G. Wen, Topological entanglement rényi entropy and reduced density matrix structure, *Phys. Rev. Lett.* **103**, 261601 (2009).

[3] J. Eisert, M. Cramer, and M. B. Plenio, Colloquium: Area laws for the entanglement entropy, *Rev. Mod. Phys.* **82**, 277 (2010).

[4] A. Kitaev and J. Preskill, Topological entanglement entropy, *Phys. Rev. Lett.* **96**, 110404 (2006).

[5] H. Li and F. D. M. Haldane, Entanglement spectrum as a generalization of entanglement entropy: Identification of topological order in non-abelian fractional quantum hall effect states, *Phys. Rev. Lett.* **101**, 010504 (2008).

[6] M. Levin and X.-G. Wen, Detecting topological order in a ground state wave function, *Phys. Rev. Lett.* **96**, 110405 (2006).

[7] G. Vidal, J. I. Latorre, E. Rico, and A. Kitaev, Entanglement in quantum critical phenomena, *Phys. Rev. Lett.* **90**, 227902 (2003).

[8] A. Hamma, R. Ionicioiu, and P. Zanardi, Ground state entanglement and geometric entropy in the kitaev model, *Physics Letters A* **337**, 22 (2005).

[9] S. Yao and Z. Wang, Edge states and topological invariants of non-hermitian systems, *Phys. Rev. Lett.* **121**, 086803 (2018).

[10] C. H. Lee and R. Thomale, Anatomy of skin modes and topology in non-hermitian systems, *Phys. Rev. B* **99**, 201103 (2019).

[11] F. Song, S. Yao, and Z. Wang, Non-hermitian skin effect and chiral damping in open quantum systems, *Phys. Rev. Lett.* **123**, 170401 (2019).

[12] R. Lin, T. Tai, L. Li, and C. H. Lee, Topological non-hermitian skin effect, *Frontiers of Physics* **18**, 53605 (2023).

[13] H. Jiang, L.-J. Lang, C. Yang, S.-L. Zhu, and S. Chen, Interplay of non-hermitian skin effects and anderson localization in nonreciprocal quasiperiodic lattices, *Phys. Rev. B* **100**, 054301 (2019).

[14] K. Zhang, Z. Yang, and C. Fang, Correspondence between winding numbers and skin modes in non-hermitian systems, *Phys. Rev. Lett.* **125**, 126402 (2020).

[15] K. Yokomizo and S. Murakami, Non-bloch band theory of non-hermitian systems, *Phys. Rev. Lett.* **123**, 066404 (2019).

[16] K. Kawabata, K. Shiozaki, M. Ueda, and M. Sato, Symmetry and topology in non-hermitian physics, *Phys. Rev. X* **9**, 041015 (2019).

[17] H.-Y. Wang, F. Song, and Z. Wang, Amoeba formulation of non-bloch band theory in arbitrary dimensions, *Phys. Rev. X* **14**, 021011 (2024).

[18] Z. Yang, K. Zhang, C. Fang, and J. Hu, Non-hermitian bulk-boundary correspondence and auxiliary generalized brillouin zone theory, *Phys. Rev. Lett.* **125**, 226402 (2020).

[19] L. Li, S. Mu, C. H. Lee, and J. Gong, Quantized classical response from spectral winding topology, *Nature Communications* **12**, 5294 (2021).

[20] X.-Q. Sun, P. Zhu, and T. L. Hughes, Geometric response and disclination-induced skin effects in non-hermitian systems, *Phys. Rev. Lett.* **127**, 066401 (2021).

[21] K. Zhang, Z. Yang, and C. Fang, Universal non-hermitian skin effect in two and higher dimensions, *Nature Communications* **13**, 2496 (2022).

[22] R. Shen and C. H. Lee, Non-hermitian skin clusters from strong interactions, *Communications Physics* **5**, 238 (2022).

[23] H. Jiang and C. H. Lee, Dimensional transmutation from non-hermiticity, *Phys. Rev. Lett.* **131**, 076401 (2023).

[24] T. Tai and C. H. Lee, Zoology of non-hermitian spectra and their graph topology, *Phys. Rev. B* **107**, L220301 (2023).

[25] R. Shen, T. Chen, B. Yang, and C. H. Lee, Observation of the non-hermitian skin effect and fermi skin on a digital quantum computer (2023), arXiv:2311.10143 [quant-ph].

[26] N. Okuma and M. Sato, Non-hermitian topological phenomena: A review, *Annual Review of Condensed Matter Physics* **14**, 83 (2023).

[27] G.-G. Liu, S. Mandal, P. Zhou, X. Xi, R. Banerjee, Y.-H. Hu, M. Wei, M. Wang, Q. Wang, Z. Gao, H. Chen, Y. Yang, Y. Chong, and B. Zhang, Localization of chiral edge states by the non-hermitian skin effect, *Phys. Rev. Lett.* **132**, 113802 (2024).

[28] Z. Lei, C. H. Lee, and L. Li, Activating non-hermitian skin modes by parity-time symmetry breaking, *Communications Physics* **7**, 100 (2024).

[29] D. C. Brody, Biorthogonal quantum mechanics, *Journal of Physics A: Mathematical and Theoretical* **47**, 035305 (2013).

[30] F. K. Kunst, E. Edvardsson, J. C. Budich, and E. J. Bergholtz, Biorthogonal bulk-boundary correspondence in non-hermitian systems, *Phys. Rev. Lett.* **121**, 026808 (2018).

[31] M. V. Berry, Physics of nonhermitian degeneracies, *Czechoslovak Journal of Physics* **54**, 1039 (2004).

[32] Z. Gong, Y. Ashida, K. Kawabata, K. Takasan, S. Higashikawa, and M. Ueda, Topological phases of non-hermitian systems, *Phys. Rev. X* **8**, 031079 (2018).

[33] N. Moiseyev, *Non-Hermitian Quantum Mechanics* (Cambridge University Press, 2011).

[34] P.-Y. Chang, J.-S. You, X. Wen, and S. Ryu, Entanglement spectrum and entropy in topological non-hermitian systems and nonunitary conformal field theory, *Phys. Rev. Res.* **2**, 033069 (2020).

[35] C. H. Lee, Exceptional bound states and negative entanglement entropy, *Phys. Rev. Lett.* **128**, 010402 (2022).

[36] Y.-T. Tu, Y.-C. Tzeng, and P.-Y. Chang, Rényi entropies and negative central charges in non-Hermitian quantum systems, *SciPost Phys.* **12**, 194 (2022).

[37] M. Fossati, F. Ares, and P. Calabrese, Symmetry-resolved entanglement in critical non-hermitian systems, *Phys. Rev. B* **107**, 205153 (2023).

[38] F. Rottoli, M. Fossati, and P. Calabrese, Entanglement hamiltonian in the non-hermitian ssh model, *Journal of Statistical Mechanics: Theory and Experiment* **2024**, 063102 (2024).

[39] G. Lee, T. Jin, Y.-X. Wang, A. McDonald, and A. Clerk, Entanglement phase transition due to reciprocity breaking without measurement or postselection, *PRX Quantum* **5**, 010313 (2024).

[40] I. Peschel, Calculation of reduced density matrices from correlation functions, *Journal of Physics A: Mathematical and General* **36**, L205 (2003).

[41] An analogous expression also holds for free bosons:  $S_{A,boson}^{(n)} = \frac{1}{n-1} \text{Tr} \left[ \log \left( \tilde{P}^n - (\tilde{P} - I)^n \right) \right]$ .

[42]  $\eta$  can be viewed as a variant of the Petermann factor [82–84].

[43] Such that the discrete momentum takes values of  $k = \pi/L, 3\pi/L, \dots$ , avoiding the singular  $k = 0$  point exactly.

[44] 2 topological bands are sufficient, since the NHSE pushes both of them onto the same boundary and makes them overlap significantly.

[45] C. M. Bender, M. V. Berry, and A. Mandilara, Generalized pt symmetry and real spectra, *Journal of Physics A: Mathematical and General* **35**, L467 (2002).

[46] C. E. Rüter, K. G. Makris, R. El-Ganainy, D. N. Christodoulides, M. Segev, and D. Kip, Observation of parity-time symmetry in optics, *Nature Physics* **6**, 192 (2010).

[47] R. El-Ganainy, K. G. Makris, M. Khajavikhan, Z. H. Musslimani, S. Rotter, and D. N. Christodoulides, Non-hermitian physics and pt symmetry, *Nature Physics* **14**, 11 (2018).

[48] M. Yang and C. H. Lee, Percolation-induced  $\mathcal{PT}$  symmetry breaking, *Phys. Rev. Lett.* **133**, 136602 (2024).

[49] S. Longhi, Non-bloch-band collapse and chiral zener tunneling, *Phys. Rev. Lett.* **124**, 066602 (2020).

[50] G.-F. Guo, X.-X. Bao, and L. Tan, Non-hermitian bulk-boundary correspondence and singular behaviors of generalized brillouin zone, *New Journal of Physics* **23**, 123007 (2021).

[51] M. Stålhammar and E. J. Bergholtz, Classification of exceptional nodal topologies protected by  $\mathcal{PT}$  symmetry, *Phys. Rev. B* **104**, L201104 (2021).

[52] M. M. Denner, T. Neupert, and F. Schindler, Infernal and exceptional edge modes: non-hermitian topology beyond the skin

effect, *Journal of Physics: Materials* **6**, 045006 (2023).

[53] R. Islam, R. Ma, P. M. Preiss, M. Eric Tai, A. Lukin, M. Rispoli, and M. Greiner, Measuring entanglement entropy in a quantum many-body system, *Nature* **528**, 77 (2015).

[54] A. J. Daley, H. Pichler, J. Schachenmayer, and P. Zoller, Measuring entanglement growth in quench dynamics of bosons in an optical lattice, *Phys. Rev. Lett.* **109**, 020505 (2012).

[55] M. B. Hastings, I. González, A. B. Kallin, and R. G. Melko, Measuring rényi entanglement entropy in quantum monte carlo simulations, *Phys. Rev. Lett.* **104**, 157201 (2010).

[56] A. K. Ekert, C. M. Alves, D. K. L. Oi, M. Horodecki, P. Horodecki, and L. C. Kwek, Direct estimations of linear and nonlinear functionals of a quantum state, *Phys. Rev. Lett.* **88**, 217901 (2002).

[57] H. Pichler, L. Bonnes, A. J. Daley, A. M. Läuchli, and P. Zoller, Thermal versus entanglement entropy: a measurement protocol for fermionic atoms with a quantum gas microscope, *New Journal of Physics* **15**, 063003 (2013).

[58] H. Buhrman, R. Cleve, J. Watrous, and R. de Wolf, Quantum fingerprinting, *Phys. Rev. Lett.* **87**, 167902 (2001).

[59] N. M. Linke, S. Johri, C. Figgatt, K. A. Landsman, A. Y. Matsurra, and C. Monroe, Measuring the rényi entropy of a two-site fermi-hubbard model on a trapped ion quantum computer, *Phys. Rev. A* **98**, 052334 (2018).

[60] Q. Wang, J. Guan, J. Liu, Z. Zhang, and M. Ying, New quantum algorithms for computing quantum entropies and distances, *IEEE Transactions on Information Theory* **70**, 5653–5680 (2024).

[61] H.-C. Chang, H.-C. Hsu, and Y.-C. Lin, Probing entanglement dynamics and topological transitions on noisy intermediate-scale quantum computers (2024), arXiv:2406.10159 [quant-ph].

[62] S. Salek, R. Schubert, and K. Wiesner, Negative conditional entropy of postselected states, *Phys. Rev. A* **90**, 022116 (2014).

[63] S.-H. Lin, R. Dilip, A. G. Green, A. Smith, and F. Pollmann, Real- and imaginary-time evolution with compressed quantum circuits, *PRX Quantum* **2**, 010342 (2021).

[64] T. Chen, R. Shen, C. H. Lee, and B. Yang, High-fidelity realization of the AKLT state on a NISQ-era quantum processor, *SciPost Phys.* **15**, 170 (2023).

[65] H. Häffner, W. Hänsel, C. F. Roos, J. Benhelm, D. Chek-al kar, M. Chwalla, T. Körber, U. D. Rapol, M. Riebe, P. O. Schmidt, C. Becher, O. Gühne, W. Dür, and R. Blatt, Scalable multiparticle entanglement of trapped ions, *Nature* **438**, 643 (2005).

[66] G. Torlai, G. Mazzola, J. Carrasquilla, M. Troyer, R. Melko, and G. Carleo, Neural-network quantum state tomography, *Nature Physics* **14**, 447 (2018).

[67] C. Kokail, R. van Bijnen, A. Elben, B. Vermersch, and P. Zoller, Entanglement hamiltonian tomography in quantum simulation, *Nature Physics* **17**, 936 (2021).

[68] Z.-K. Lin, Y. Zhou, B. Jiang, B.-Q. Wu, L.-M. Chen, X.-Y. Liu, L.-W. Wang, P. Ye, and J.-H. Jiang, Measuring entanglement entropy and its topological signature for phononic systems, *Nature Communications* **15**, 1601 (2024).

[69] J. Zhao, B.-B. Chen, Y.-C. Wang, Z. Yan, M. Cheng, and Z. Y. Meng, Measuring rényi entanglement entropy with high efficiency and precision in quantum monte carlo simulations, *npj Quantum Materials* **7**, 69 (2022).

[70] N. Goldman, J. C. Budich, and P. Zoller, Topological quantum matter with ultracold gases in optical lattices, *Nature Physics* **12**, 639 (2016).

[71] A. Aspuru-Guzik and P. Walther, Photonic quantum simulators, *Nature Physics* **8**, 285 (2012).

[72] J. Li, A. K. Harter, J. Liu, L. de Melo, Y. N. Joglekar, and L. Luo, Observation of parity-time symmetry breaking transitions in a dissipative floquet system of ultracold atoms, *Nature Communications* **10**, 855 (2019).

[73] M. Z. Hasan and C. L. Kane, Colloquium: Topological insulators, *Rev. Mod. Phys.* **82**, 3045 (2010).

[74] N. P. Armitage, E. J. Mele, and A. Vishwanath, Weyl and dirac semimetals in three-dimensional solids, *Rev. Mod. Phys.* **90**, 015001 (2018).

[75] P. Calabrese and J. Cardy, Entanglement entropy and quantum field theory, *Journal of Statistical Mechanics: Theory and Experiment* **2004**, P06002 (2004).

[76] C. Holzhey, F. Larsen, and F. Wilczek, Geometric and renormalized entropy in conformal field theory, *Nuclear Physics B* **424**, 443 (1994).

[77] M. B. Hastings, An area law for one-dimensional quantum systems, *Journal of Statistical Mechanics: Theory and Experiment* **2007**, P08024 (2007).

[78] This is particularly so if the exceptional dispersion is square-root, as for some generalizations of our model in Methods, subsection A.1.

[79] M. M. Denner, A. Skurativska, F. Schindler, M. H. Fischer, R. Thomale, T. Bzdušek, and T. Neupert, Exceptional topological insulators, *Nature Communications* **12**, 5681 (2021).

[80] F. Zhang, The schur complement and its applications (2005).

[81] C. H. Lee, L. Li, R. Thomale, and J. Gong, Unraveling non-hermitian pumping: Emergent spectral singularities and anomalous responses, *Phys. Rev. B* **102**, 085151 (2020).

[82] J. Wiersig, Petermann factors and phase rigidities near exceptional points, *Phys. Rev. Res.* **5**, 033042 (2023).

[83] Y.-Y. Zou, Y. Zhou, L.-M. Chen, and P. Ye, Detecting bulk and edge exceptional points in non-hermitian systems through generalized petermann factors, *Frontiers of Physics* **19**, 23201 (2023).

[84] H. Wang, Y.-H. Lai, Z. Yuan, M.-G. Suh, and K. Vahala, Petermann-factor sensitivity limit near an exceptional point in a brillouin ring laser gyroscope, *Nature Communications* **11**, 1610 (2020).

### Acknowledgments

We thank Ruizhe Shen and Linhu Li for helpful discussions. This work is supported by the National Research Foundation, Singapore under its QEP2.0 programme (NRF2021-QEP2-02-P09) as well as the Ministry of Education, Singapore (MOE award number: MOE-T2EP50222-0003).